CrossMark

Evidence for a Sub-Chandrasekhar-mass Type Ia Supernova in the Ursa Minor Dwarf Galaxy

Andrew McWilliam[1], Anthony L. Piro[1], Carles Badenes[2] , and Eduardo Bravo[3]
[1] The Observatories of the Carnegie Institution for Science, 813 Santa Barbara Street, Pasadena, CA 91101, USA
andy@carnegiescience.edu, piro@carnegiescience.edu
[2] Department of Physics and Astronomy, University of Pittsburgh, 3941 O'Hara Street, Pittsburgh, PA 15260, USA; badenes@pitt.edu
[3] E.T.S. Arquitectura del Vallés, Universitat Politécnica de Catalunya, Carrer Pere Serra 1-15, E-08173 Sant Cugat del Vallés, Spain; eduardo.bravo@upc.edu

Abstract

A long-standing problem is identifying the elusive progenitors of Type Ia supernovae (SNe Ia), which can roughly be split into Chandraksekhar and sub-Chandrasekhar-mass events. An important difference between these two cases is the nucleosynthetic yield, which is altered by the increased neutron excess in Chandrasekhar progenitors due to their pre-explosion simmering and high central density. Based on these arguments, we show that the chemical composition of the most metal-rich star in the Ursa Minor dwarf galaxy, COS 171, is dominated by nucleosynthesis from a low-metallicity, low-mass, sub-Chandrasekhar-mass SN Ia. Key diagnostic abundance ratios include Mn/Fe and Ni/Fe, which could not have been produced by a Chandrasekhar-mass SN Ia. Large deficiencies of Ni/Fe, Cu/Fe and Zn/Fe also suggest the absence of alpha-rich freeze-out nucleosynthesis, favoring low-mass white dwarf progenitors of SNe Ia, near $0.95\,M_\odot$, from comparisons to numerical detonation models. We also compare Mn/Fe and Ni/Fe ratios to the recent yields predicted by Shen et al., finding consistent results. To explain the [Fe/H] at -1.35 dex for COS 171 would require dilution of the SN Ia ejecta with $\sim 10^4\,M_\odot$ of material, which is expected for an SN remnant expanding into a warm interstellar medium with $n \sim 1\,\mathrm{cm}^{-3}$. In the future, finding more stars with the unique chemical signatures we highlight here will be important for constraining the rate and environments of sub-Chandrasekhar SNe Ia.

Key words: galaxies: dwarf – nuclear reactions, nucleosynthesis, abundances – stars: abundances – supernovae: general

1. Introduction

The low average metallicity of most dwarf galaxies suggests that, like the Milky Way (MW) halo, star formation (SF) was truncated in these systems prior to complete gas consumption, presumably due to gas loss (e.g., Hartwick 1976). Thus, dwarf galaxies offer the potential to study the early phases of chemical enrichment.

In the Type Ia supernova (henceforth SN Ia) time-delay picture of chemical evolution (e.g., Matteucci & Brocato 1990, henceforth MB90), dwarf galaxies experience a low specific star formation rate (SFR), resulting in an increased fraction of nucleosynthesis products from SN Ia versus core-collapse Type II supernovae (henceforth SNe II), compared to the MW at any given metallicity. In this scenario, MB90 predicted that dwarf galaxies would show low $[\alpha/\mathrm{Fe}]$[4] ratios compared to MW disk, due to enhanced iron production from SN Ia without extra α-element synthesis from SN II. These low $[\alpha/\mathrm{Fe}]$ ratios were subsequently observed (e.g., Shetrone et al. 2001, 2003). Enhanced SN Ia material in the Carina dwarf galaxy was claimed by Venn et al. (2012) and Norris et al. (2017), based on detailed chemical abundance measurements and comparison to theoretical supernova yields.

Thus, it appears that dwarf galaxies are enhanced in SN Ia ejecta; so, the chemical composition of stars in these systems may be employed as probes of SN Ia nucleosynthesis and thereby provide constraints on the SN Ia mechanism.

For recent reviews of SN Ia scenarios and variants, including nucleosynthesis predictions, see Seitenzahl & Townsley (2017) and Maoz et al. (2014). One long-standing scenario for SN Ia involves an explosion following the transfer of mass from a companion onto a white dwarf (WD) near the Chandrasekhar-mass limit (e.g., Whelan & Iben 1973).

As first noted by Arnett (1971), iron-peak nucleosynthesis depends strongly on the neutron excess,[5] η, during explosion; in particular, the yields for neutron-rich species like ^{51}V, ^{55}Mn, and ^{58}Ni are reduced at low neutron-excess values.

Timmes et al. (2003) suggested that a dispersion of SN Ia metallicities could be responsible for much of the intrinsic variation in the luminosity of SN Ia, due to the dependence of explosively produced ^{56}Ni on the neutron excess, which changes markedly with metallicity.

Density-dependent electron captures in the central region of a Chandrasekhar-mass SN Ia increases the core η above that due to the original stellar metallicity, when densities exceed $\sim 2 \times 10^8\,\mathrm{g\,cm}^{-3}$ (e.g., Khokhlov 1991; Maeda et al. 2010). This core neutronization resulted in the predicted ^{54}Fe/^{56}Fe ratios of Khokhlov (1991) being much higher than the solar value for pure detonations and pure deflagrations; only the predictions for delayed detonation Chandrasekhar-mass SN Ia fit the solar isotopic ratio.

---

[4] The bracket notation indicates $\log_{10}$ number ratio relative to solar abundance: $[X/Y] = \log_{10}(N(X)/N(Y)) - \log_{10}(N(X)/N(Y))_\odot$.

---

[5] $\eta = (N - Z)/(N + Z)$, where N and Z are the neutron and proton numbers, respectively.

In addition to this increase in the core η during the explosion, detailed nucleosynthesis calculations for Chandrasekhar-mass SN Ia scenarios (e.g., Chamulak et al. 2008; Piro & Bildsten 2008; Martínez-Rodríguez et al. 2016; and Piersanti et al. 2017) showed that for ~1000 years prior to the SN Ia explosion, low-level convective core carbon burning, or simmering, occurs, which increases η to a value roughly equivalent to half the solar composition. In particular, the Piersanti et al. (2017) calculations show that very low-metallicity Chandrasekhar-mass SN Ia have a floor in η at the time of explosion near $\eta = 6.7 \times 10^{-4}$; however, at higher metallicity, SNe Ia show correspondingly larger η. Thus, even with the η increase due to simmering, SN Ia nucleosynthesis yields reflect their original metallicity. However, the basic conclusion from these studies is that all Chandrasekhar-mass SNe Ia experience pre-explosion simmering with an increase to high η.

Thanks to this increased η, even quite metal-poor Chandrasekhar-mass WDs produce SN Ia Mn/Fe and Ni/Fe yield ratios that are not too different from the solar values.

Alternate SN Ia scenarios (e.g., Iben & Tutukov 1984; Webbink 1984; Fink et al. 2007) involve detonation following rapid helium accretion or a violent collision, or merger, of two sub-Chandrasekhar-mass WDs (the double-degenerate scenario), ultimately triggering a detonation in the primary. Importantly, the simmering phase does not occur in these sub-Chandrasekhar-mass models, so there can be no pre-explosion increase in η beyond that provided by the primordial metallicity, unlike the Chandrasekhar-mass models. Furthermore, according to Seitenzahl et al. (2013), the critical density required to produce ^{55}Mn following normal freeze-out after nuclear statistical equilibrium ($\rho \geqslant 2 \times 10^8 \, \mathrm{g \, cm^{-3}}$) is not reached for WD masses below ~$1.2 \, M_\odot$, suggesting no Mn production in sub-Chandrasekhar-mass models. Contrary to this assertion, however, the 0.88 to $1.15 \, M_\odot$ sub-Chandrasekhar-mass SN Ia models of E. Bravo (introduced in Yamaguchi et al. 2015) show a factor of 10 range in both Mn/Fe and Ni/Fe yield ratios, depending on initial mass and metallicity; these results are confirmed in the recent work of Shen et al. (2017).

Notwithstanding these details, low-metallicity sub-Chandrasekhar-mass SN Ia are expected to produce very low Mn/Fe and Ni/Fe ratios, distinctly lower than the near-solar values expected from Chandrasekhar-mass SN Ia. Thus, the Mn/Fe and Ni/Fe yield ratios are intimately related to the SN Ia mechanism and may be employed for diagnostic purposes.

While direct measurement of iron-peak element ratios ratios in supernova remnants (SNRs; e.g., Badenes et al. 2008a; Yamaguchi et al. 2015; Martínez-Rodríguez et al. 2017) provides a way to probe the SN Ia mechanism (e.g., Bravo 2013), the important role of SN Ia in the chemical evolution of dwarf galaxies suggests that the composition of these systems may also be of use (e.g., North et al. 2013; Kobayashi et al. 2015). We may expect chemical signatures from SNe Ia to be enhanced in low-metallicity, low-mass, dwarf galaxies, where the chemical enrichment by SNe II is truncated and small numbers of SNe could potentially have a significant and measurable effect on chemical composition. Based on progenitor lifetimes, the order of iron-peak nucleosynthesis might reasonably be: SN II, followed by Chandrasekhar-mass SN Ia, and finally sub-Chandrasekhar-mass SN Ia. Thus, one might expect that the most metal-rich stars in a dwarf galaxy are more likely to result from chemical enrichment phase of sub-Chandrasekhar-mass SNe Ia.

This work was motivated by the unusual composition of the most metal-rich star, COS 171, in the Ursa Minor dwarf galaxy (henceforth UMi), as measured by Cohen & Huang (2010; henceforth CH10). We compare the chemical composition of COS 171 to other UMi stars and the MW halo. Accordingly, we identify a chemically normal star, UMi 28104, useful as a standard to isolate the composition of the contamination event that produced COS 171. We confirm the published local thermodynamic equilibrium (LTE) abundance calculations of CH10, and when possible, we have applied differential non-LTE corrections. After comparison of our final chemical abundance ratios with predicted yields from a variety of SN nucleosynthesis scenarios, we conclude that the COS 171 composition resulted from a low-mass, metal-poor, sub-Chandrasekhar-mass SN Ia event. In a chemical evolution context, this is most easily understood as due to a sub-Chandrasekhar-mass SN Ia diluted with ~$10^4 \, M_\odot$ of hydrogen, consistent with expectations for an SNR expanding into a warm interstellar medium.

2. The Chemical Composition of Ursa Minor

The detailed chemical composition of stars in UMi has been investigated by Shetrone et al. (2001), Sadakane et al. (2004), and CH10.

The seminal work of Shetrone et al. (2001) found that the chemical compositions of UMi and the Draco and Sextans dSphs are characterized by a large dispersion in [Fe/H], low [α/Fe] and [Y/Fe] ratios, and [Ba/Eu] ratios indicating r-process nucleosynthesis. Thus, the UMi chemical composition is distinct from the MW halo.

Sadakane et al. (2004) confirmed the low [α/Fe] ratios in UMi, and, for one star near [Fe/H] $= -1.5$, found very strong overabundances of neutron-capture elements, matching the solar system r-process pattern.

The most extensive detailed chemical composition study of UMi was undertaken by CH10, who examined 10 UMi RGB stars. They found a range in [Fe/H] from -3.10 to -1.35 dex, roughly normal O/Fe, Mg/Fe, and Si/Fe for the most metal-poor UMi stars, but generally declining [α/Fe] with increasing metallicity, well below the MW halo trend, particularly for stars above [Fe/H] ~ -2. Critically, three of the four most metal-rich UMi stars show [Eu/Fe] above $+0.60$ dex (but up to $+0.87$ dex), and all four stars above [Fe/H] $= -1.9$ show heavy-element ratios consistent with pure r-process composition. In this way, UMi is similar to the r-process dwarf galaxy Reticulum II (Ret II; Ji et al. 2016), although Ret II has a higher [r/Fe].

2.1. The Unusual UMi Star COS 171

At [Fe/H] $= -1.35$ dex, the most metal-rich star in the CH10 sample, COS 171, has an extraordinary chemical composition, including large deficiencies (exceeding 0.6 dex) of the [C/Fe], [Na/Fe], [Sc/Fe], [V/Fe], [Mn/Fe], [Ni/Fe], [Cu/Fe], and [Zn/Fe] ratios, as well as subsolar ratios, below -0.3 dex, for [Mg/Fe], [Ca/Fe], [Ti/Fe], [Cr/Fe], and [Co/Fe].

In the following discussion of COS 171, we consider only the UMi abundance results of CH10 in order to avoid complications from systematic measurement differences between studies.

Figure 1 shows [X/Fe] versus [Fe/H] in UMi for the sample of stars studied by CH10, shown with small red crosses,
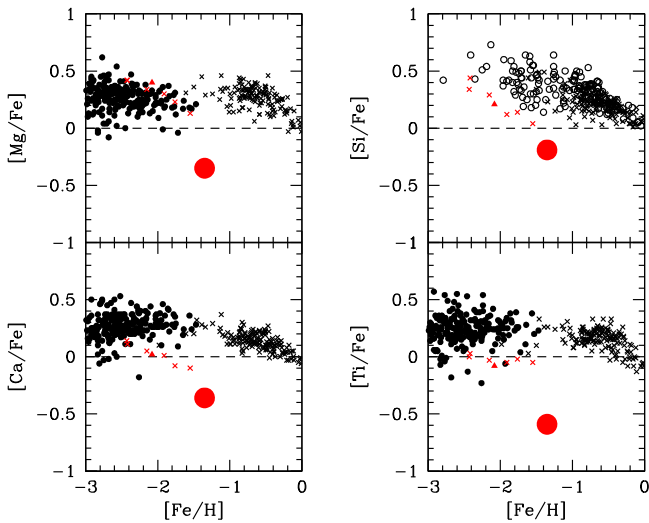
Figure 1. [α/Fe] ratios in UMi (red) compared to the MW (black) halo, and thin and thick disks. The large filled red circle indicates the UMi star COS 171, while small red crosses show other UMi stars from Cohen & Huang (2010). The small red filled triangle is our standard star UMi 28104. Black crosses indicate MW thin and thick disk stars, and some halo stars, from Reddy et al. (2006); black filled circles are MW metal-poor halo stars from Barklem et al. (2005); black open circles show [Si/Fe] for MW halo and disk stars from Fulbright (2000). In the standard chemical evolution paradigm of Matteucci & Brocato (1990), the low [α/Fe] ratios suggest heavy contamination by SN Ia ejecta in UMi, compared to the MW, increasing with increasing [Fe/H].

Figure 2. Iron-peak [X/Fe] ratios in UMi compared to the MW halo, and thin and thick disks. Symbols are the same as in Figure 1. COS 171 has among the lowest [X/Fe] ratios reported for the odd-numbered elements Sc, V, Mn, and Cu.

compared to the MW halo, and thick and thin disks (black symbols). It is immediately obvious that UMi shows depleted [α/Fe] ratios, with a general trend that is qualitatively consistent with the scenario of MB90, in which dwarf galaxies are predicted to show the decline in [α/Fe] at lower [Fe/H] than the MW due to reduced SFR. Since this reduction of [α/Fe] is thought to be due to the contribution of iron from SNe Ia, the UMi stars appear to show an increasing, and relatively large, SN Ia/SN II ratio. Notably, the most iron-rich star in UMi, COS 171 (shown as the large filled red circle), exhibits extraordinarily low [α/Fe] ratios compared to any MW study.

On closer inspection, Figure 1 shows that, excluding the most metal-rich star in UMi, the [Mg/Fe] ratios in UMi are not as depleted as the [Si/Fe], [Ca/Fe], and [Ti/Fe] ratios; indeed, the [Mg/Fe] ratios appear normal compared to the MW halo (again, except for the most metal-rich UMi star). If [α/Fe] deficiencies in dwarf galaxies are supposed to be due to a reduced SFR resulting from excess SN Ia iron at low [Fe/H], as predicted by MB90, then the halo-like [Mg/Fe] in UMi stars is unexpected: naively, all [α/Fe] ratios should decline together.

The implied [Mg/Ca] enhancement, near +0.3–0.4 dex, might be explained by an overrepresentation of massive SNe II. Much larger [Mg/Ca] ratios, near +0.95 dex, have been seen in the Hercules dwarf (henceforth Her) by Koch et al. (2008). Because Mg production is made almost exclusively by massive core-collapse SN II events with progenitor masses exceeding $\sim 30\,M_\odot$ (e.g., Woosley & Weaver 1995), the high [Mg/Ca] ratios in Her indicate enhanced pollution by high-mass SN II events. Koch et al. (2008) suggested that for Her, this could result from stochastic sampling of the initial mass function (henceforth IMF) that, by chance, favored massive stars. However, the probability of randomly selecting only massive stars, above $30\,M_\odot$, from the IMF diminishes rapidly with the
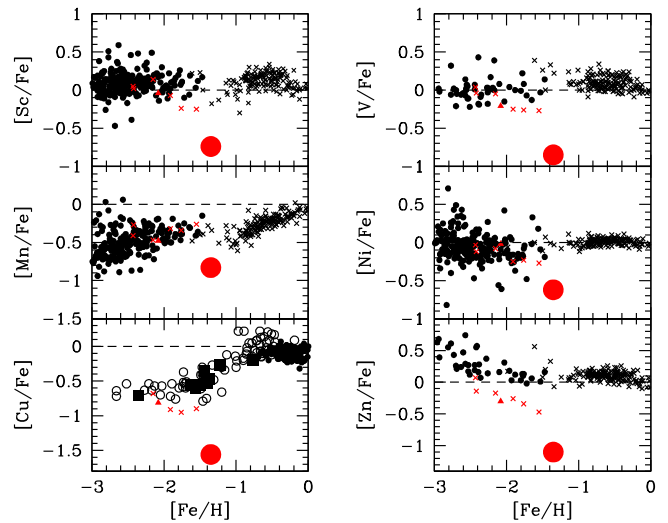
number of samplings. Such a mechanism could only occur if a small number of SN II events (fewer than 11) produced the Her chemical composition. Similarly, the enhanced [Mg/Ca] ratios in UMi may be the signature of the stochastic sampling of the SN II IMF in the chemical evolution of this dwarf galaxy.

We note that in Figure 1 the [Mg/Fe] ratio for COS 171 is markedly lower than would be extrapolated from the trend at lower [Fe/H]. Indeed, while the bulk of UMi stars show [Mg/Ca] $\sim$ +0.3 dex, for COS 171, [Mg/Ca] = +0.0 dex. This suggests some production of Ca in the composition of COS 171.

The iron-peak elements in Figure 2 show generally good agreement with the MW stars, but severe underabundances for the most metal-rich UMi star, COS 171. In particular, the odd-numbered elements Sc, V, Mn, and Cu are neutron-rich, so their deficiency suggests a rather low neutron excess, η (or equivalently, high electron fraction, Y_e).

It occurs to us that the excessively low [X/Fe] ratios for 10 of the 27 measured elements in COS 171, shown in Figures 1 and 2, might be largely explained by the addition of nearly pure iron to a pre-existing composition. In Figures 3 and 4, we show the UMi [X/H] versus [Fe/H] LTE abundances from CH10; some panels show a 1:1 line. It is clear from these figures that a simple shift to lower [Fe/H] by ~ 0.7 dex would bring the COS 171 [X/H] ratios into approximate consistency with the more metal-poor members of the galaxy, at least for Na, Mg, Sc, Cu, Ni, Zn, Y, and Ba.

Figures 3 and 4 suggest that COS 171 resulted from ~ 0.7 dex of Fe added to the pre-existing galaxy composition. Given that the COS 171 [Fe/H] = −1.35 dex, a pre-existing composition of [Fe/H] ~ -2.05 dex is suggested. The CH10 star with metallicity closest to our putative pre-existing composition is UMi 28104, at [Fe/H] = −2.08 dex. Because UMi 28104 has a composition similar to the more metal-poor stars in UMi, with abundance ratios fairly typical of dwarf galaxy stars in other systems (e.g., Shetrone et al. 2001), we take the chemical composition of UMi 28104 to indicate that of UMi just prior to the enrichment event that produced COS 171.

Figure 5 shows the abundance ratios of COS 171 relative to the standard, UMi 28104 (i.e., this is the difference in log
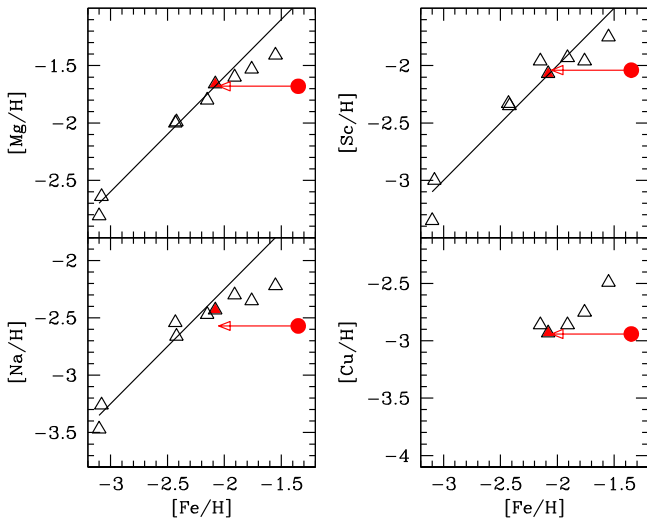
Figure 3. [X/H] vs. [Fe/H] for Mg, Na, Sc, and Cu in UMi, reported by Cohen & Huang (2010). For these elements, the composition of the highest [Fe/H] star, COS 171 (filled red circle), more closely resembles UMi stars near [Fe/H] = −2.0 dex. The red filled triangle indicates our standard star UMi 28104. The red arrow indicates the effect of a reduction in [Fe/H] by 0.7 dex, which suggests that the COS 171 composition resulted from the addition of 0.7 dex of iron-peak material to a pre-existing mixture. The black line for Mg, Na, and Sc indicates a 1:1 relation between [X/H] and [Fe/H].
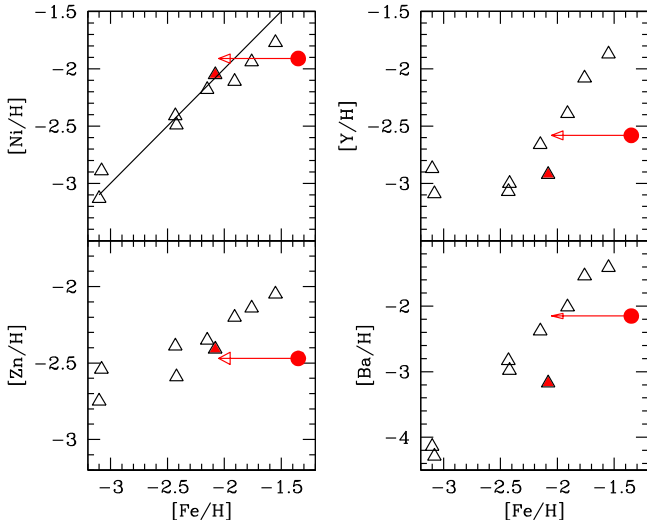

Figure 4. [X/H] vs. [Fe/H] for Ni, Zn, Y, and Ba in UMi, reported by Cohen & Huang (2010). The composition of the highest [Fe/H] star, COS 171 (filled red circle), more closely resembles UMi stars near [Fe/H] = −2.0 dex, even for the neutron-capture elements, but with an [Fe/H] enhancement near 0.7 dex. The red arrow indicates the effect of a reduction in [Fe/H] by 0.7 dex. The black line indicates a 1:1 relation between [Ni/H] and [Fe/H]. The red filled triangle indicates our standard star UMi 28104.

abundances); we emphasize that this is not the difference in the number of atoms.

The abundance ratios in Figure 5 not only highlight the enhanced elements in COS 171, but thanks to the similar stellar atmosphere parameters of UMi 28104, they also mitigate a number of systematic measurement errors (e.g., *gf* values, systematic model atmosphere errors, non-LTE effects, temperature-scale errors, etc.). However, random errors due to EW measurement and abundance scatter due to random atmosphere parameter uncertainties persist. While the abundance ratios in Figure 5 are based on the CH10 LTE abundances, the points in
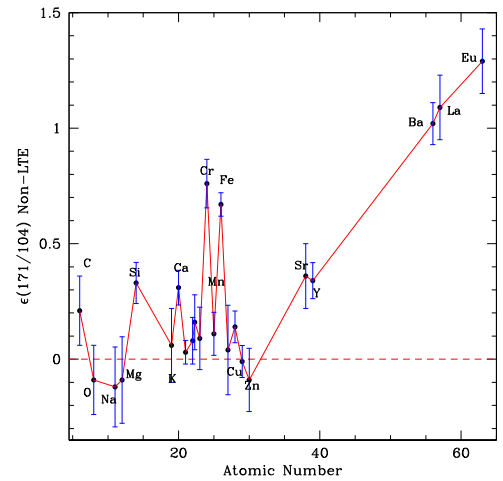

Figure 5. Abundance distribution ratio (difference in the log), $\Delta\varepsilon(171-28104)$, including non-LTE corrections (see Section 2.4). The unusual composition of UMi star #171 is evident. This figure includes revised abundances for O and K, based on our re-analysis of the CH10 spectra. Error bars indicate 1σ error on the mean difference derived from the rms abundance dispersions given by CH10, plus the effect of random errors on the atmosphere parameters; however, the uncertainty for oxygen, based on a single line for both stars, was estimated from the EW uncertainty.

the figure have been corrected for differential non-LTE effects, whenever possible (see Section 2.4).

Error bars in Figure 5 were taken from the abundance dispersions given by CH10, or in the case of oxygen from the EW uncertainties, combined in quadrature with random errors arising from uncertainties in the spectroscopic stellar atmosphere parameters, as indicated by the CH10 Fe I abundances. The main difference between the ratios presented in Figure 5 compared to the CH10 LTE results is for Mn: with non-LTE corrections, the Mn enhancement in COS 171, at +0.11 dex, is only 1.2σ from zero, whereas the uncorrected CH10 result is +0.38 dex. In Figure 5, the displayed oxygen abundance ratio is not from CH10, but indicates the value found in this work (see Section 2.3) from the original CH10 spectra. Thus, we find no oxygen enhancement for COS 171 relative to UMi 28104, whereas the original CH10 results suggested an oxygen abundance for COS 171 higher by 0.31 dex.

Figure 5 shows strong enhancements of neutron-capture elements (i.e., elements heavier than zinc), increasing with increasing atomic number, which appears to be due to an r-process enrichment event that affected all UMi stars above [Fe/H] ∼ −1.9 dex. Since three such r-process rich stars do not share the unusual iron-peak composition of COS 171, we assume that the r-process enrichment event was an unrelated phenomenon.

Excluding the neutron-capture elements, Figure 5 shows clear detection of Si, Ca, Cr, and Fe enhancements in COS 171, well above the individual measurement uncertainties. Marginal detections, comparable to the estimated error bars, occur for C, Ti, V, Mn, and Ni, while O, Na, Mg, K,[6] Sc, Co, Cu, and Zn show no evidence for enhancement.

2.2. A Check on the LTE Results

As a check on the CH10 results, for UMi 28104 and the unusual UMi star COS 171, we have employed the CH10

---

[6] Based on our re-analysis of the K abundance for COS 171.

equivalent widths (EWs) and atmosphere parameters to compute element abundances, using the 2014 version of the LTE spectrum synthesis program MOOG (Sneden 1973). Our abundances are in very good agreement with CH10, including the excitation temperatures derived from Fe I lines, thus supporting the unusual composition of COS 171 claimed by CH10.

2.3. Oxygen and Potassium Re-analysis

The CH10 abundance of oxygen in COS 171 was based on only two lines: [O I] at 6363 Å and O I at 7771 Å, with putative EWs of 12.6 mÅ and 8.5 mÅ; for UMi 28104, only the 6363 Å line was measured, with an EW of 8.8 mÅ. These EWs are strongly affected by noise, given the 1σ EW uncertainty of ~4 mÅ, which explains the large abundance difference derived from the two lines in COS 171.

Curiously, the [O I] line at 6300 Å, which has a larger gf value than the 6363 Å line (roughly three times stronger), was not employed by CH10.

In our comparisons of observed and predicted yields from a variety of nucleosynthesis sites, the CH10 oxygen abundance showed significant discordance with abundances of other elements, such as Mg. We therefore elected to re-analyze the original CH10 Keck/HIRES spectra of COS 171 and UMI 28104, which we downloaded from the Keck Archive.[7] Reduction to one-dimensional spectra was performed using the program *makee*, and EWs were measured with the IRAF *splot* routine.

These spectra show that the 6363 Å [O I] and O I 7771 Å lines are, indeed, extremely noisy in COS 171 and UMi 28104. The [O I] line at 6300 Å has a significant EW and should be readily measured; however, in the CH10 UMi spectra, this line is blended with a comparable telluric O_2 intercombination (P7) line from the (2–0) b–X $^1\Sigma_g^+$–$^3\Sigma_g^-$ electronic vibration–rotation transition. This telluric blend suggests why CH10 did not employ the [O I] 6300 Å line. In UMi 28104, the [O I]/O_2 blend at 6300 Å has a total EW of 42.8 mÅ, while for COS 171 the feature has a total EW of 35.8 mÅ. We estimated the strength of the blending telluric O_2 line from the EW of its spin doublet, located 0.78 Å redward. The two P7 spin-doublet lines have very similar, but not identical, EWs in telluric standard spectra of hot stars, and the redder of the doublet lines is unblended in the UMi stellar spectra. We computed the strength ratio of the O_2 line pair from a high S/N spectrum of a telluric standard B star, which then enabled the strength of the O_2 contamination of the [O I] 6300 Å feature to be computed from the unblended O_2 line.

For UMi 28104, the telluric-corrected [O I] 6300 Å EW is 21.8 mÅ, while for COS 171 the line is weaker, at 12.1 mÅ. Incidentally, these values suggest 6363 Å [O I] line EWs of 7 and 4 mÅ, respectively (compared to the CH10 values of 8.8 and 12.6 mÅ). Thus, the 6363 Å lines are too weak compared to the measurement uncertainty, of $1\sigma \sim 4$ mÅ, to allow reliable oxygen abundance measurement. For this reason, we rely only on the [O I] line at 6300 Å for oxygen abundances in the UMi stars.

Oxygen abundances were computed here from our telluric-corrected EWs for the [O I] 6300 Å line, using the spectrum synthesis program MOOG (Sneden 1973), the stellar model atmosphere grid of Kurucz,[8] and the atmosphere parameters given

in CH10. We find an [O/H] of −1.616 and −1.712 dex for UMi 28104 and COS 171, respectively, on the meteoritic solar abundance scale of Asplund et al. (2009). Curiously, COS 171 has a lower [O/H], by 0.10 dex, despite its significantly higher [Fe/H], but since this oxygen abundance difference is within the measurement uncertainty of 0.15 dex, the two stars might reasonably have the same oxygen abundance.

We also employed the CH10 spectra to check the measured EW for critical species, including potassium, for which only the K I line at 7699.0 Å was used to determine potassium abundances. We measured a K I line EW of 105 mÅ for COS 171, which is significantly smaller than the 130 mÅ in CH10. Unfortunately, we find no reasonable explanation for the difference, since the data appear to be completely inconsistent with the high published EW. However, we confirmed the CH10 K I line EW for UMi 28104, at 109 mÅ. Our K I EW measurement resulted in a decreased potassium abundance for COS 171, at $\varepsilon(K) = 3.28$ dex, which is within 0.01 dex of the value found for UMi 28104. Thus, there appears to have been no measurable potassium production by the progenitor event of COS 171.

2.4. Non-LTE Effects and Abundance Uncertainties

Our use of star UMi 28104 as a comparison to COS 171 both accounts for the pre-existing UMi composition present in COS 171 and eliminates constant systematic effects, such as log gf scales.

One important correction enabled by taking differences between COS 171 and UMi 28014 is that these stars are both metal-poor RGB stars and both likely suffer similar non-LTE effects on the derived LTE abundances. Thus, to first order, the non-LTE effects cancel out when comparing COS 171 to UMI 28104, but because the latter is more metal-poor, by ~0.7 dex, differential non-LTE effects are possible. In particular, non-LTE effects are typically more extreme in more metal-poor stellar atmospheres (e.g., Asplund 2005; Collet et al. 2005).

We refer the reader to Asplund (2005) for a review of non-LTE effects in stellar atmospheres, as well as computational aspects, caveats, and limitations due to the paucity of known collisional rates.

In order to evaluate the differential non-LTE abundance corrections, and thus compare the abundances here with predicted nucleosynthetic yields, we have searched the literature for non-LTE abundance corrections appropriate for the COS 171 and UMi 28104 atmosphere parameters; this includes the lines used for the abundances of each element. Unfortunately, not all lines of all elements have been investigated, and we could not find non-LTE calculations for vanadium.

Incomplete coverage of stellar atmosphere parameter space is a problem that prevents us from estimating the differential non-LTE abundance corrections between COS 171 and UMi 28104 for some elements; for example, the focus on warm dwarfs in Yan et al. (2015, 2016) prevents reliable differential non-LTE abundance corrections for copper.

In Table 1 we list non-LTE corrections for a variety of species in COS 171 and UMi 28104; when possible, we have preferred results from Bergemann[9] and collaborators, because that group's results include more species than other studies. We

Table 1
Adopted Non-LTE Corrections (dex)

Species	COS 171	UMi 28104	Notes
Na I	−0.00	−0.02	1
Mg I	−0.06	+0.01	2
Si I	−0.02	−0.02	3
K I	−0.30	−0.37	4
Ca I	+0.10	+0.15	5
Sc II	0.00	0.00	6
Ti I	+0.24	+0.39	7
Ti II	0.00	0.00	8
V I	⋯	⋯	9
Cr I	+0.04:	+0.04:	10
Mn I	+0.15	+0.42	11
Fe I	+0.05	+0.11	12
Co I	+0.19	+0.42	13
Ni I	0.00	0.00	14
Cu I	0.2:	0.2:	15
Zn I	−0.13	−0.10	16

Note. When possible, the non-LTE corrections are taken from the MPIA non-LTE Web page (http://nlte.mpia.de/) of Bergemann, which was used for O, Mg, Si, Ti, Mn, Fe, and Co. For Na, we employed the non-LTE Web page INSPECT, http://inspect.coolstars19.com/, of Lind. For Ca, we used the non-LTE Web page of Mashonkina, http://spectrum.inasan.ru/nLTE/. Source references are cited in these Web pages, but are not always correct, or may not contain information given by the Web page. 1. Average Na I corrections are −0.057 and −0.087 for 171 and 104 if Na D lines included. 2. See Bergemann et al. (2016) and also Osorio & Barklem (2016) and Mashonkina (2013). 3. Si corrections in the MPIA Web page are not given in the identified reference. 4. Non-LTE corrections for the K I line at 7699 Å estimated from Ivanova & Shimanskiĭ (2000). 5. Ca non-LTE corrections given by Mashonkina et al. (2016). 6. Sc II non-LTE corrections not found, but assumed to be zero or very small. 7. For Ti I source, the reference is Bergemann (2011), but see also Mashonkina et al. (2016). 8. Ti II non-LTE corrections from Mashonkina et al. (2016) are negligibly small. 9. We could not find non-LTE corrections for vanadium. 10. Lawler et al. (2017) found non-LTE corrections for Cr near +0.04 dex in the metal-poor dwarf HD 84937. Bergemann & Cescutti (2010) also presented Cr non-LTE corrections for dwarf stars. 11. MPIA Web page cites Mn non-LTE corrections from Bergemann & Gehren (2008). 12. MPIA Web page cites Fe non-LTE corrections from Bergemann et al. (2012). 13. MPIA Web page cited cobalt non-LTE corrections from Bergemann et al. (2010). 14. Wood et al. (2014) found no evidence of non-LTE effect on Ni in the metal-poor dwarf HD 84937. 15. Our estimated Cu non-LTE corrections are based on calculations for metal-poor dwarf stars by Yan et al. (2015, 2016) see also Shi et al. (2014). 16. Zinc non-LTE corrections estimated from metal-poor dwarf calculations by Takeda et al. (2005), who assumed no collisions with hydrogen, $S_H = 0$.

make no evaluation of which source of non-LTE corrections is more reliable.

Fortunately, the non-LTE correction differences in Table 1 for most elements are less than 0.10 dex, with the exception of those derived from lines of Ti I, Mn I, and Co I. Since the yield of Mn is sensitive to the neutron excess during explosive nucleosynthesis, it is a useful element for diagnostic purposes; however, unfortunately, Mn abundances suffer from very large non-LTE corrections.

As Table 1 shows, the Fe I non-LTE abundance corrections for COS 171 are smaller than those for UMi 28104, in the same sense as a number of other species; this mitigates, to a small extent, the deviation of the non-LTE corrected [X/Fe I] ratios from the LTE values.

In Table 2, we present our final adopted LTE abundances, non-LTE corrections, and random 1σ X/Fe abundance uncertainties for COS 171 and UMi 28104. The random X/Fe abundance

uncertainties were based on the reported abundance dispersions from CH10 combined in quadrature with the abundance errors due to 1σ random T_{eff} and microturbulent velocity uncertainties of 30 K and 0.05 km s^{-1}, respectively (random gravity and metallicity uncertainties have negligible effect so were ignored). These 1σ spectroscopic parameter uncertainties were deduced here from the 1σ uncertainties in the slope of CH10 Fe I abundance correlations with excitation potential and equivalent width, respectively.

Table 2 constitutes the abundance data for comparison with a variety of explosive stellar nucleosynthesis scenarios used in this work.

3. Comparison with Nucleosynthesis Predictions

In this section, we compare the chemical composition of COS 171 with predicted nucleosynthesis yields from a variety of supernova scenarios. In a first step, we simply make a table comparison of the raw LTE and non-LTE corrected COS 171 abundances for a few diagnostic elements. Then for the most promising scenarios, we compare the detailed COS 171 composition to theoretical yields added to the composition of our standard star, UMi 28104, which we have assumed to represent the background composition enriched by the COS 171 progenitor. This has the advantage that zero-point measurement errors common to COS 171 and UMi 28104 cancel out, giving the smallest measurement uncertainty; however, differential metallicity effects may still be present. Finally, we compare the theoretical yields for sub-Chandrasekhar-mass SN Ia and Chandrasekhar-mass SN Ia deflagration to detonation transition (DDT) models to the composition of COS 171 with the UMi 28104 background composition subtracted out. While this gives a direct comparison with predicted yields, the uncertainties in the measured abundance differences can be large, especially for elements with small or zero enhancement over the background composition.

All three comparisons favor a sub-Chandrasekhar-mass SN Ia as the progenitor of the COS 171 composition.

3.1. Comparison of Supernova Yields with the Measured COS 171 Composition

In Table 3, we compare the raw LTE and non-LTE corrected [X/Fe] ratios of a handful of diagnostic elements in COS 171 with predicted element yields for various explosive events.

For core-collapse SN II yields, we compare with the predictions of Woosley & Weaver (1995, henceforth WW95) and Kobayashi et al. (2006, henceforth K06); for pair instability supernova (PISN) predictions, at $Z = 0$, we compare with the results of Heger & Woosley (2002, henceforth HW02), while for $Z = 0.001$ PISNe, we use the result of Kozyreva et al. (2014). For predicted SN Ia yields of various masses and metallicities, we consider the Chandrasekhar-mass DDT models of Badenes et al. (2003, 2008b)[10] and Yamaguchi et al. (2015), and the sub-Chandrasekhar-mass models of E. Bravo (2016, private communication; henceforth the Bravo models) introduced in Yamaguchi et al. (2015), calculated with a version of the code described in Bravo & Martínez-Pinedo (2012).[11] In particular, we seek predicted yields that could

---

[10] Element yields from the DDT SN Ia models of Badenes et al. (2003, 2008b) are provided in Appendix A of this paper in Tables 4–7.
[11] The Bravo sub-Chandrasekhar-mass SN Ia yields are tabulated in Tables 8–11 in Appendix B of this paper.

Table 2
Adopted Abundances (dex)

Species	UMi 28104			Cos 171		
	$\varepsilon(X)_{LTE}$	$\Delta\varepsilon_{nlte}$	$\sigma(X/Fe)_{rand.}$	$\varepsilon(X)_{LTE}$	$\Delta\varepsilon_{nlte}$	$\sigma(X/Fe)_{rand.}$
C	5.97	⋯	0.15	6.18	⋯	0.15
O I	7.07	0.0	0.11	6.98	0.0	0.13
Na I	3.84	−0.02	0.13	3.70	+0.00	0.10
Mg I	5.87	+0.01	0.10	5.85	−0.06	0.16
Si I	5.68	−0.02	0.08	6.01	−0.02	0.06
K I	3.29	−0.37	0.10	3.65	−0.30	0.10
Ca I	4.30	+0.15	0.04	4.66	+0.10	0.05
Sc II	0.98	⋯	0.06	1.01	⋯	0.06
Ti I	2.83	+0.39	0.04	3.06	+0.24	0.04
Ti II	3.08	⋯	0.07	3.24	⋯	0.07
V I	1.71	⋯	0.09	1.80	⋯	0.06
Cr I	3.22	+0.04	0.04	3.98	+0.04	0.07
Mn I	2.83	+0.42	0.10	3.21	+0.15	0.06
Fe I	5.37	+0.11	⋯	6.10	+0.05	⋯
Co I	2.94	+0.42	0.11	3.21	+0.19	0.10
Ni I	4.15	+ 0.0	0.04	4.29	+0.0	0.04
Cu I	1.32	+0.2	0.10	1.31	+0.2	0.10
Zn I	2.22	−0.10	0.14	2.16	−0.13	0.11
Sr II	0.57	⋯	0.11	0.93	⋯	0.10
Y II	−0.75	⋯	0.07	−0.41	⋯	0.07
Ba II	−0.99	⋯	0.07	0.03	⋯	0.08
La II	−1.97	⋯	0.11	−0.88	⋯	0.10
Eu II	−2.31	⋯	0.11	−1.02	⋯	0.10

Table 3
Diagnostic Element Ratios from Supernovae

	[C/Fe]	[Si/Fe]	[Ca/Fe]	[V/Fe]	[Cr/Fe]	[Mn/Fe]	[Ni/Fe]
COS 171 (LTE)	−0.90	−0.15	−0.28	−0.81	−0.31	−0.92	−0.56
COS 171 (NLTE)	−0.95	−0.22	−0.23	⋯	−0.32	−0.82	−0.56
SN Ia (DDTa) $Z = 0.01$	−3.30	−0.65	−0.27	−0.76	−0.11	−0.19	−0.07
SN II (WW95) $Z = 0.01\,Z_\odot$							
$12\,M_\odot$	−0.51	−0.46	−0.46	−1.11	−0.46	−0.80	+0.01
$15\,M_\odot$	−0.34	−0.14	−0.13	−0.69	−0.17	−0.60	−0.06
$20\,M_\odot$	+0.18	+0.75	+0.69	+0.03	+0.49	−0.19	−1.07
SN II (K06) $Z = 0$							
$13\,M_\odot$	−0.16	+0.33	+0.11	−0.40	+0.08	−0.54	−0.30
$20\,M_\odot$	−0.07	+0.48	+0.40	−0.42	+0.35	−0.31	−0.79
SN Ia (Sub-Ch)							
$0.88\,M_\odot$							
$Z = 0.00025$	−2.16	−0.19	+0.21	−1.47	+0.30	−1.56	−2.47
$Z = 0.0025$	−2.16	−0.17	+0.19	−0.92	+0.30	−0.39	−1.76
$0.97\,M_\odot$							
$Z = 0.00025$	−2.61	−0.45	−0.05	−1.57	+0.01	−1.77	−0.63
$Z = 0.0025$	−2.61	−0.44	−0.08	−1.17	+0.01	−0.69	−0.63
$1.06\,M_\odot$							
$Z = 0.00025$	−3.00	−0.71	−0.24	−1.67	−0.20	−1.87	−0.60
$Z = 0.0025$	−3.00	−0.69	−0.29	−1.37	−0.20	−0.90	−0.60
PISN (HW02) $Z = 0$							
$242\,M_\odot$	−1.14	+0.25	+0.13	−1.16	+0.04	−0.74	−0.29
$260\,M_\odot$	−1.38	+0.02	−0.08	−1.38	−0.15	−0.95	−0.09
PISN (KYL14) $Z = 0.001$							
$250\,M_\odot$	−1.60	+0.31	+0.46	−0.96	+0.14	−0.56	−0.39

potentially reproduce the unusually low [Mn/Fe], [Ni/Fe], and [α/Fe] ratios seen in COS 171, as displayed in Figures 1 and 2.

From Table 3, one can immediately see that massive (e.g., ⩾20 $M_\odot$), core-collapse SNe II fail to reproduce the COS 171

composition because of their expected large α-element yields (e.g., Si, Ca); the situation would be worse for more massive SNe II, especially for [Mg/Fe], which is overproduced in very massive SNe II (e.g., WW95, K06). Table 3 shows that

7

massive SN II also overproduce C, V, Cr, and Mn relative to COS 171.

Low-mass SNe II, such as the $12\,M_\odot$ and $13\,M_\odot$ models of WW95 and K06, respectively, produce low enough α-elements to be consistent with COS 171, but they still significantly overproduce carbon and nickel relative to COS 171. We note that the yields for $Z = 0$, $10\,M_\odot$ SNe II predicted by Heger & Woosley (2010) indicate [Ni/Fe] ratios close to the solar value, well above the measured COS 171 value at -0.56 dex.

For PISNe, the $Z = 0$ HW02 $260\,M_\odot$ [X/Fe] yields for C, Si, Ca, V, Cr, and Mn are fairly close to the low values seen in COS 171, but the predicted [Ni/Fe] ratio is too high by more than ~ 0.5 dex. The $250\,M_\odot$, $Z = 0.001$ PISN model of Kozyreva et al. (2014) gives a very poor match to COS 171, and in particular cannot explain the low X/Fe values for Si, Ca, Cr, Mn, and possibly Ni.

For the DDTa Chandrasekhar-mass SN Ia model, Table 3 shows that C/Fe, Si/Fe, and Ca/Fe ratios are low enough to fit COS 171, but Cr/Fe, Mn/Fe, and Ni/Fe fail significantly.

The sub-Chandrasekhar Bravo models indicate Mn and Ni abundances low enough to match the observed COS 171 Mn/Fe and Ni/Fe ratios for almost all models presented. The $1.06\,M_\odot$ sub-Chandrasekhar-mass model predicts [X/Fe] suitably low for all diagnostic species listed in Table 3, except for chromium, where the measured [Cr/Fe] ratio exceeds the prediction by 1.5σ times the random measurement uncertainty.

3.2. Comparison with Chandrasekhar-mass SNe Ia

Predicted yields for DDT models added to the UMi 28104 background composition, at two deflagration to detonation transition densities (DDTa and DDTc; e.g., Badenes et al. 2003, 2008b), and a range of metallicities are shown in Figure 6. We note that the neutron-excess increase due to the pre-explosion simmering phase (e.g., Piro & Bildsten 2008) was not included in these calculations. Thus, the large increase in neutron excess due to the pre-explosion carbon-burning simmering phase neutronization does not occur in these models. However, efficient neutron captures do occur close to the center of the WD during the early deflagration phase of the explosion, despite the relatively low initial central density near $2 \times 10^9\,\mathrm{g\,cm^{-3}}$, and is the likely source of Mn production of these incomplete models.

In the study of Piersanti et al. (2017), which included the simmering effect, the neutron excess at explosion for their lowest metallicity DDT models always exceeds 0.668×10^{-3}, equivalent to a metallicity of $z \sim 0.007$. Thus, the Badenes et al. (2003, 2008b) DDT model predictions with metallicity less than $z \sim 0.007$ (giving the lowest predicted Mn/Fe ratios) are not expected to occur.

Generally, however, the Badenes et al. (2003, 2008b) DDT models give fair agreement with the measured non-LTE-corrected COS 171 composition. However, the important neutron-rich elements Mn and Ni are significantly overproduced, compared to COS 171, well beyond the measurement uncertainties (even when simmering effects are ignored); Cr/Fe is also poorly fit.

Badenes et al. (2003, 2008b) did not compute Na or K yields, so Figure 6 shows, with red lower limits, the [Na/Fe] and [K/Fe] ratios expected for no production in the COS 171 progenitor; here, the final [Na/Fe] and [K/Fe] ratios are due to the UMi 28104 background composition diluted with 0.7 dex of extra Fe.
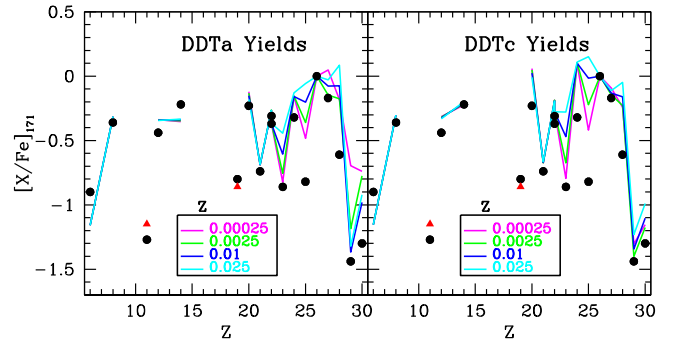

Figure 6. Comparison of the COS 171 non-LTE-corrected composition (filled black circles), from C to Zn, with Badenes et al. (2003, 2008b) Chandrasekhar-mass nucleosynthesis yields, for various metallicities and two model deflagration to detonation transition densities (DDTa and DDTc) added to the background composition of UMi 28104 (solid lines). Red lower limit triangles are shown for Na and K, which were not reported by Badenes et al. (2003, 2008b), indicating the [Na/Fe] and [K/Fe] ratios for zero production of these elements. The predicted [Mn/Fe] yields fail to reproduce the low values seen in COS 171, and [Ni/Fe] ratios are overproduced in the models, both by ~ 0.5 dex, compared to the observations; these differences are well in excess of the ~ 0.1 dex measurement uncertainties. The [Si/Fe], [Ca/Fe], and [Cr/Fe] ratios are better matched by the DDTa model. The two measured [Ti/Fe] points (at $Z = 22$) indicate Ti I and Ti II.

A range of Chandrasekhar-mass, single-degenerate SN Ia models, investigated by Dave et al. (2017), permits some comparison with the composition of COS 171. Although Dave et al. (2017) did not publish their yields, their Figures 4 and 7 contains yield information for a few elements. In particular, their Figure 4 allows a comparison of the predicted X/Fe mass fractions for Ni, Mn, and Cr as a function of WD metallicity for all classes of models considered; also, their Figure 7 allows an approximate comparison for their standard deflagration model and their high-density, low C/O ratio deflagration to detonation model.

Surprisingly, we found that the Mn/Fe and Cr/Fe mass ratios for the zero-metallicity, high-density, gravitationally confined detonation ($z = 0$, GCD-HIGHDEN) model in Dave et al. (2017), Figure 4, provide a reasonable match to the measured Mn/Fe and Cr/Fe mass ratios in COS 171. However, the predicted Ni/Fe mass fractions for all models were factors of 12 to 60 greater than those measured for COS 171, with the closest match given by the GCD-HIGHDEN model. The STD-DEF and DDT-HIGHDEN-LOWC/CENTRAL models in Dave et al. (2017) compared badly with COS 171, with Mn/Fe and Ni/Fe much larger than observed, by approximately a factor of 10; however, Cr/Fe was reasonably well matched by these models.

We conclude that none of the single-degenerate models match the observed composition of COS 171; in particular, the predicted Mn/Fe and Ni/Fe ratios appear to rule out this scenario.

3.3. Comparison with Pair Instability Supernova Yields

Interestingly, the predicted PISN element yields, added to the UMi 28104 background composition, for the $260\,M_\odot$, $Z = 0$ star of HW02 come fairly close to fitting the measured non-LTE-corrected COS 171 X/Fe ratios for most elements, except for Ni/Fe, which is too high by more than 0.5 dex. Given the comparison in Figure 7, an extrapolation of the PISN yields to slightly higher than their maximum mass seems to do even better for all elements except Ni. However, HW02 stress that the $260\,M_\odot$ is strictly the highest possible $Z = 0$ PISN mass; above this limit, pair production is unable to provide sufficient pressure, and the object collapses to a black hole.
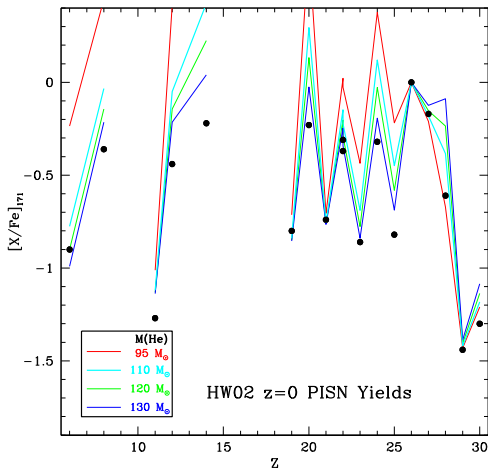
Figure 7. Comparison of the HW02 pair instability supernova element yields, added to the UMi 28104 background composition, with the COS 171 abundance distribution (including differential non-LTE corrections). The closest match is obtained for a helium-core mass of 130 $M_\odot$, corresponding to a total mass of 260 $M_\odot$; however, the [Ni/Fe] ratio for that model exceeds the measured value by $\sim$0.5 dex. The two measured [Ti/Fe] points (at $Z = 22$) indicate Ti I and Ti II.

Figure 8. Comparison of the COS 171 non-LTE-corrected composition (filled black circles), from C to Zn, with Bravo (private communication) sub-Chandrasekhar-mass nucleosynthesis yields, for various WD masses and primordial metallicities, z, added to the background composition of UMi 28104 (solid lines). The predictions show that Mn/Fe, V/Fe, and Ni/Fe are sensitive to initial metallicity, while Si/Fe, Ca/Fe, and Cr/Fe depend on WD mass. The 0.1 dex error bar in the top-left corner of the 0.88 $M_\odot$ panel indicates the quadrature sum of typical 1σ random measurement uncertainties for UMi 28104 and COS 171 [X/Fe] ratios. The two measured [Ti/Fe] points (at $Z = 22$) indicate Ti I and Ti II.

Furthermore, an improved fit with PISN yields cannot be obtained with nonzero metallicity PISN events, as indicated by the $Z = 0.001$, 250 $M_\odot$ model by Kozyreva et al. (2014), which fails to match the observed Si/Fe, Ca/Fe, Cr/Fe, Mn/Fe, and Ni/Fe in COS 171. Thus, currently predicted element yields from PISN events do not fit the composition of COS 171, and we reject this scenario.

3.4. Comparison with Sub-Chandrasekhar-mass SN Ia Bravo Models

Figure 8 shows excellent overlap between the predicted sub-Chandrasekhar-mass SN Ia yields added to the UMi 28104 background composition and the observed abundances in COS 171 (corrected for differential non-LTE effects). Critically, there is good overlap for the important [Mn/Fe] and [Ni/Fe] ratios, but also for Sc, Ti, V, and Co. In particular, the low [Mn/Fe] and [V/Fe] ratios seen in COS 171 are only reproduced in the lowest metallicity models.

Figure 8 reveals that the Bravo model sub-Chandrasekhar-mass predictions give decreasing [X/Fe] yields of Si, Ca, and Cr with increasing WD mass; conversely, the [Ni/Fe] yield increases with increasing WD mass. These trends suggest that both the WD mass and metallicity may be constrained using the full array of element ratios relative to iron.

The low [Ni/Fe], [Cu/Fe], and [Zn/Fe] ratios in COS 171, while reproduced in the 0.88 $M_\odot$, $Z = 0.00025$ Bravo model, are not well-matched with higher WD masses. However, Si is best reproduced in the 0.97 $M_\odot$ models, and Ca, Ti, and Cr abundances in COS 171 are best matched by the 1.06 $M_\odot$, $Z = 0.00025$ models. Thus, there is some disagreement between the best matching sub-Chandrasekhar WD mass depending on which elements are considered. While errors in the adopted differential non-LTE corrections to Ca, Ti, and Cr LTE abundances might resolve the mass discrepancy, the changes required are at least 0.2 dex and need to work in the same direction, which seems unlikely. Alternatively, an increase in the Fe I non-LTE correction for UMi 28104 of 0.2 dex would reduce the progenitor mass indicated by Ca, Ti, and Cr, but this would shift all solid curves in Figure 8 down, and the implied progenitor
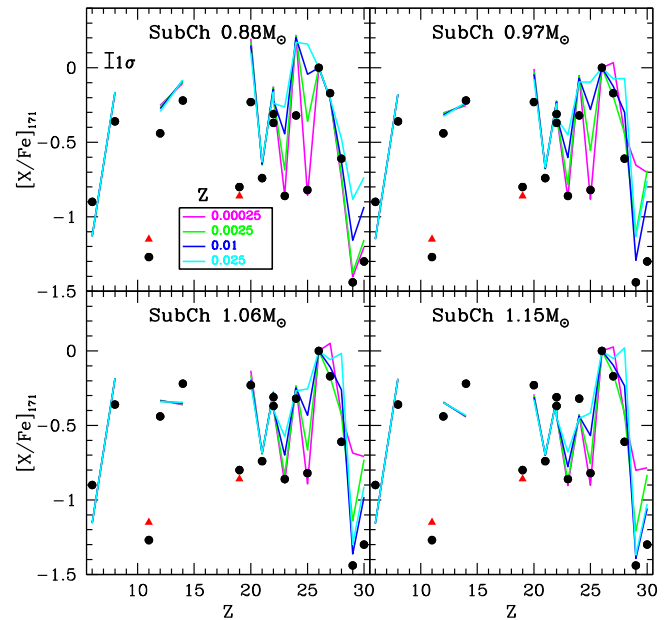
mass from Si and Ni abundances would move to even lower values, still out of agreement with Ca, Ti, and Cr.

In the Bravo models, Cu and Zn are made in two regions: by alpha-rich freeze-out in the core and also following carbon burning close to the surface, where protons and neutrons are released that subsequently build up Cu and Zn in a series of (n, γ), (p, γ), and (n, p) reactions. Importantly, the alpha-rich freeze-out cannot occur in the 0.88 $M_\odot$ model because its maximum temperature is insufficient for complete Si burning, unlike the more massive WD models (where maximum temperatures are near $T \sim 6$ GK). Furthermore, for the (n, γ) and (n, p) source of Cu and Zn near the surface, the controlling neutron excess is determined by the original stellar metallicity in the sub-Chandrasekhar-mass models. Therefore, the observed low abundances of Cu and Zn in COS 171 suggests both low metallicity ($Z = 0.00025$) and low WD mass (0.88 $M_\odot$).

Direct comparison of the background-subtracted COS 171 element mass ratios with predicted sub-Chandrasekhar-mass yields are presented in Figures 9 and 10 for Mn/Fe as a function of Ni/Fe and Si/Fe, respectively. These two figures show abundance differences, by number, between COS 171 and UMi 28104, compared to the Bravo model predictions. Because these mass ratios are based on true abundance differences, the measurement uncertainties lead to large uncertainties for elements with similar abundances in the two stars; this is despite the small abundance measurement uncertainties, near 0.1 dex, seen in Figure 8.

We estimated the relative abundance difference uncertainties in Figures 9 and 10 arising from the scatter in CH10 measurements, including covariances and random excitation temperature errors, and assuming a 0.03 dex log gf scatter.
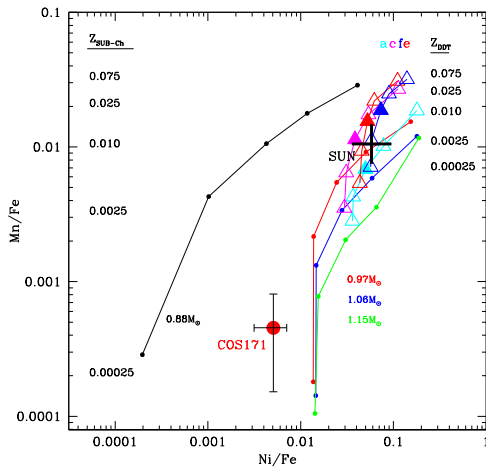
Figure 9. Estimated Ni/Fe and Mn/Fe mass ratios for the COS 171 progenitor compared to DDT and sub-Chandrasekhar-mass models. Triangles: DDT models with different deflagration to detonation transition densities (a, c, e, f) and metallicities; filled triangles indicate $Z_{DDT} = 0.010$, slightly above the effective value arising from simmering. Small filled circles connected by lines: various sub-Chandrasekhar-mass models, for different metallicities. Large filled red circle: COS 171 with the background composition of UMi 28104 subtracted. Large black cross: solar value. Note that COS 171 lies in a low-metallicity Mn/Fe region, much lower than that possible with DDT models (due to simmering increase of η); COS 171 also has low Ni/Fe, in a region sensitive to WD mass, due to the reduced role of alpha-rich freeze-out nucleosynthesis. At higher metallicity, the Ni/Fe and Mn/Fe ratios increase due to neutron-excess dependent nucleosynthesis.
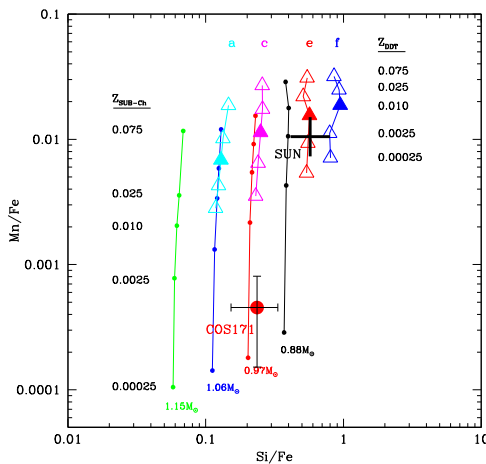

Figure 10. Estimated Si/Fe and Mn/Fe mass ratios for the COS 171 progenitor compared to DDT and sub-Chandrasekhar-mass models. Symbols are the same as in Figure 9. The Si/Fe ratio increases with decreasing WD mass, likely due to a greater fraction of the core that experiences incomplete Si burning. The Si/Fe ratio indicates a WD mass near $0.94\,M_\odot$, consistent with the value from Ni/Fe in Figure 9. Note the clean separation between WD mass and metallicity indicated by Si/Fe and Mn/Fe in this plot.

Accordingly, we found 1σ uncertainties of 0.070 dex, 0.047 dex, and 0.089 dex for for Mn/Fe, Ni/Fe, and Si/Fe, respectively. Thus, the small total relative abundance uncertainties translate into the substantial mass ratio uncertainties shown in Figures 9 and 10.

In Figure 9, the low Mn/Fe mass ratio indicates a low metallicity for the COS 171 progenitor, within 1σ of the lowest metallicity in the Bravo models, at $Z = 0.00025$, corresponding to [Fe/H] $= -1.7$ dex. Thus, the COS 171 Mn/Fe mass ratio is consistent with a low-metallicity sub-Chandrasekhar-mass SN Ia and lies well below any of the DDT model predictions.

The COS 171 Ni/Fe mass ratio in Figure 9 also lies well below the DDT models, and below most of the sub-Chandrasekhar-mass model predictions, and indicates a low WD mass between 0.97 and $0.88\,M_\odot$. We note that for the lowest WD masses considered in the Bravo models, the maximum core temperatures are insufficient to drive the alpha-rich freeze-out, which is an important source of Ni, as well as of Cu and Zn. In the Bravo models, the reduced Ni production from the alpha-rich freeze-out is likely the reason why the predicted Ni/Fe ratio declines steeply below $0.97\,M_\odot$ and at low metallicity. However, at high metallicity, there is an increase in Ni/Fe, even for the $0.88\,M_\odot$ models; this is likely due to increased neutron excess for higher metallicity sub-Chandrasekhar-mass SNe Ia.

The importance of the alpha-rich freeze-out in the production of Ni, Cu, and Zn leads to the sensitivity of these elements to the WD progenitor mass as well as to metallicity; indeed, the measured low Ni/Fe, Cu/Fe, and Zn/Fe ratios for COS 171 suggest that the progenitor was likely low mass (a linear interpolation suggests $0.95\,M_\odot$), with a reduced or no alpha-rich freeze-out and very low metallicity. The low metallicity is supported by the measured low Mn/Fe and V/Fe ratios.

Figure 10 also shows that the COS 171 composition lies outside the range of Chandrasekhar-mass SNe Ia in Table 3. Linear interpolation over Si/Fe for the sub-Chandrasekhar-mass models in Figure 10 suggests a mass of $0.94\,M_\odot$, consistent with that indicated by the Ni/Fe ratios. Contrary to the case for Ni/Fe, however, the Si/Fe ratio increases with decreasing WD mass; this is likely due to the relatively low temperatures of the low-mass models resulting in incomplete Si burning and larger amounts of unburnt Si remaining.

We can compare the subtracted COS 171 minus UMi 28104 element mass ratios with the sub-Chandrasekhar-mass SN Ia mass ratio predictions of Shen et al. (2017), appearing in their Figures 8–11. Our subtracted Mn/Fe and Ni/Fe mass ratios for COS 171 lie close to the $0.9\,M_\odot$, $Z = 0$, result of Shen et al. (2017) in their Figure 8, but suggest a mass near $0.97\,M_\odot$ in their Figure 9 (both adopt a C/O mass ratio of 50/50). On the other hand, the Shen et al. (2017) predictions for Cr/Fe mass ratios, appearing in their Figure 11, barely overlaps with the measured value for COS 171, but is best matched in their models with a WD mass of $1.1\,M_\odot$. As mentioned previously, the Bravo model Cr/Fe mass ratio predictions suggest a match to COS 171 near $1.06\,M_\odot$. Thus, both sets of sub-Chandrasekhar-mass models suffer the same differences as our best estimate for the element ratios in COS 171.

We are encouraged by the agreement between the Shen et al. (2017) and Bravo model predictions for sub-Chandrasekhar-mass SN Ia element yields of Si, Mn, Fe, and Ni; of particular significance is the implied low mass of the SN Ia progenitor, which is also supported by the large deficiencies of the alpha-rich freeze-out elements Ni, Cu, and Zn.

However, the higher mass WD progenitor indicated by the Ca/Fe, Ti/Fe, and Cr/Fe ratios suggest that details of the actual SN Ia event differed slightly from the models.

4. Chemical Evolution of UMi and COS 171

Here we discuss possible chemical evolution scenarios to explain the unusual chemical composition of COS 171 in UMi. As mentioned previously, it is clear that the composition of the slightly more metal-poor stars in UMi were not on the chemical path to COS 171. However, it appears that COS 171 resulted

from the addition of iron-peak and r-process material to the composition of UMi stars near [Fe/H] = −2 dex, similar to UMi 28104.

4.1. Contamination of an Existing Star in the Proximity of a Single SN Ia

It is possible that the unusual composition of COS 171, dominated by a sub-Chandrasekhar-mass SN Ia, may have been due to direct accretion of ejecta from a nearby supernova. In this scenario, COS 171 would have been the outer star in a triple system orbiting a pair of merging low-mass WDs. Assuming an envelope mass for COS 171 of $0.4\,M_\odot$, then at [Fe/H] = −1.35 dex, it contains $2.8 \times 10^{-5}\,M_\odot$ of iron, of which $6.3 \times 10^{-6}\,M_\odot$ was due to the pre-existing, [Fe/H] ∼ −2 dex, material. If $0.5\,M_\odot$ of Fe was produced by the SN Ia event, then a fraction of only 4.3×10^{-5} of the SN Ia iron was captured by COS 171. If COS 171 was a main-sequence star at the time of the accretion, with roughly solar radius, and assuming that the accretion radius was equal to the physical radius, then COS 171 must have been separated from the SN Ia event by $\sim 76\,R_\odot$, roughly 0.4 au, in order to reach [Fe/H] = −1.35 dex. This distance is smaller than the radius of the RGB star phase of the WD progenitors, and so seems unlikely.

On the other hand, if COS 171 was an RGB star, of $20\,R_\odot$ radius, at the time of accretion, then the separation from the SN Ia event would have been approximately 7 au, which is larger than the maximum radius of the AGB phase (roughly 1.5 au) of the progenitor WDs. These separations seem small considering that the merger of two WDs would be required for the SN Ia event in an even smaller region, and must also have accommodated the previous RGB and AGB phases for both WD progenitors. Thus, if this mechanism did occur, there may well have been a reduction in the size of the COS 171 orbit prior to the accretion and supernova event. Furthermore, in the RGB accretion scenario, the SN Ia event must have occurred relatively recently. Given these constraints, we do not favor this scenario.

4.2. Contamination of a Typical Molecular Cloud by Many SNe Ia

In order to reach the chemical composition of COS 171 via pollution of a giant molecular cloud near $10^6\,M_\odot$, ejecta from approximately 100 SNe Ia are required. The difficulty with such a scenario is that with many SNe, one might expect to see an averaging of element yields from other nucleosynthesis events, in particular SNe II and Chandrasekhar-mass SNe Ia, in which case the unusual abundance ratios seen in COS 171 might not be expected. For such a scenario, a systematic modulation of the polluting supernova ejecta appears to be necessary in order to obtain the COS 171 composition, which is dominated by sub-Chandrasekhar-mass SN Ia ejecta.

To circumvent this problem, one could propose that only sub-Chandrasekhar-mass SNe Ia occurred during a late phase of chemical enrichment in UMi, perhaps from the last epoch of iron-peak enrichment by the longest-lived progenitors, which led to the SN Ia in UMi being dominated by the merger of sub-Chandrasekhar-mass WD stars.

Evidence for large-scale enrichment by low-metallicity sub-Chandrasekhar-mass SN Ia in other dwarf galaxies could be construed, qualitatively, from the deficiencies of V, Mn, Co, Ni, Cu, and Zn, relative to Fe, in the Sagittarius dwarf galaxy obtained by Hasselquist et al. (2017), Sbordone et al. (2007), and McWilliam et al. (2003); from the Ni deficiencies in LMC stars found by Van der Swaelmen et al. (2013); and from the Ni deficiencies in the Fornax dwarf galaxy by Letarte et al. (2010). However, the element deficiencies in these dwarf galaxies are much less extreme than those seen in COS 171, as if mixing with a range of supernova yields occurred in these systems, unlike in COS 171.

Detailed investigation into the less extreme deficiencies, seen elsewhere, is required before they are taken as solid evidence of sub-Chandrasekhar-mass SN Ia nucleosynthesis; they likely require dilution with element yields from other supernova types. Thus, it is possible that sub-Chandrasekhar-mass SN Ia nucleosynthesis is common among dwarf galaxies, and therefore that a sub-Chandrasekhar-mass SN Ia dominated phase might have occurred in UMi, but it is not yet proven.

In this pollution scenario, we would expect many other stars sharing the chemical composition of COS 171 to be present in UMi; such objects may yet be found among the lower luminosity UMi stars. Indeed, the frequency of stars in UMi that share the chemical composition of COS 171 would provide strong constraints on the three scenarios outlined here.

4.3. Contamination of Interstellar Gas by a Single SN Ia

One possibility is that the iron-peak composition of COS 171 resulted from the pollution of interstellar gas by a single SN Ia event. Since individual SN Ia events typically yield approximately $0.5\,M_\odot$ of iron, this must be diluted with $\sim 9000\,M_\odot$ of [Fe/H] = −2 dex gas, in order to reach the COS 171 metallicity, at [Fe/H] = −1.35 dex. This amount of gas dilution corresponds to a relatively low-mass molecular cloud.

Detailed modelling of the evolution of SNR by Chevalier (1974) show that the amount of interstellar material (ISM) swept up by an SNR depends on many factors, including the energy of the explosion, the density of the ISM, the strength of the local magnetic fields, and cooling from metals and grains.

Equations describing SNR growth, in Chevalier (1974), indicate that at an ISM density of $1.0\,\mathrm{cm}^{-3}$ (characteristic of the warm ISM), the typical SNR shell velocity drops to the dispersion of interstellar clouds at a radius near 44 pc, indicating a swept-up mass of $10^4\,M_\odot$. This is completely consistent with the detailed SNR treatment of Cioffi et al. (1988), also including metal-dependent cooling, which gives a radius of 42 pc, again with an implied swept-up mass near $10^4\,M_\odot$.

A more recent calculation, by Asvarov (2014), is also consistent with these results, and estimated the largest SNR radius of 45 pc for a remnant expanding into an ISM with uniform density of $1.0\,\mathrm{cm}^{-3}$, over 4×10^5 yr. A radius of 34 pc was found when the magnetic field pressure was increased by a factor of 4. Notably, Asvarov (2014) employed a relatively small critical velocity, at Mach 2.

These predictions are consistent with the distribution of SNR sizes in nearby galaxies, for example as found by Badenes et al. (2010), who found a sharp cutoff at a radius near 30 pc and the largest SNR radii near 60 pc.

The formation of molecular clouds out of enriched warm interstellar gas is the subject of ongoing research (e.g., see Vázquez-Semadeni et al. 2007); however, it appears that molecular clouds are short-lived objects within an ongoing equilibrium process of rapid formation by gravitational

instability and equally rapid disruption by stellar feedback (e.g., Mac Low et al. 2017).

Given these considerations, it seems reasonable that as UMi ran out of gas and star formation in the galaxy drew to a close, a single, stochastic, event might have enriched $10^4\,M_\odot$ of warm interstellar gas, all or part of which subsequently formed into a star-forming molecular cloud, producing the last few stars in UMi, including COS 171. Such an event might be more likely to result from a long-lived progenitor, delayed from a previous star formation epoch, such as a sub-Chandrasekhar-mass SN Ia. Given the requirement of mixing the SN Ia ejecta with $\sim 10^4\,M_\odot$ of hydrogen in order to produce COS 171, and that this is the natural outcome for an SNR mixing into warm interstellar gas, this is our favored scenario for the origin of COS 171.

This scenario for the origin of COS 171 suggests that stochastic chemical enrichment occurred in the high-metallicity phase of UMi evolution. Recent work by Cescutti & Kobayashi (2017) compared the trend of reported [Mn/Fe] with [Fe/H] in UMi. While they found that DDT models gave the best fit for chemical evolution through homogeneous enrichment, a model of stochastic chemical enrichment, including nucleosynthesis products from at least two SN Ia types (SN Iax and sub-Chandrasekhar-mass SN Ia), gives the best fit to the observed dispersion in [Mn/Fe]. While their conclusion is completely consistent with the result found here, their fit to the dispersion requires a reliable estimate of the [Mn/Fe] measurement uncertainties. On the other hand, the highly unusual abundance ratios in COS 171, as discussed in this work, cannot reasonably be explained by measurement error.

The idea of stochastic chemical enrichment for the Carina dwarf galaxy was put forward by Venn et al. (2012) in order to explain their stellar abundance patterns. Remarkably, their most metal-rich star, Car 612, has highly unusual chemical abundance patterns and a similar [Fe/H] to UMi COS 171, near -1.3 dex, suggesting the possibility that this object also formed from the enrichment of warm ISM by a single SN Ia event.

5. Summary

We have investigated the highly unusual chemical composition, found by CH10, of star COS 171 in the UMi dwarf galaxy. We confirm the stellar atmosphere parameters and LTE iron and other element abundances found by CH10, based on their published EWs. However, for oxygen abundances, we employ the 6300 Å [O I] line from the CH10 spectra, corrected for telluric contamination. We also revise the potassium abundance in COS 171 down by 0.37 dex, based on an EW remeasurement of the somewhat saturated K I line at 7699.0 Å in the CH10 spectrum.

The composition of COS 171 is unlike any MW halo star, with uniquely low X/Fe ratios for O, Mg, Si, Ca, Ti, Sc, V, Mn, Ni, Cu, and Zn. Abundance ratio plots reveal that this unusual chemical composition seems to result from the addition of ~ 0.7 dex of iron-peak material to a pre-existing composition, near [Fe/H] $= -2.05$ dex. Other UMi stars, slightly more metal-poor than COS 171, do not share the same iron-peak chemical locus, although an r-process enrichment in those stars is also seen in COS 171. The r-process enrichment appears to be disconnected and separate from the iron-peak peculiarity of COS 171.

We adopt the star UMi 28104, with [Fe/H] $= -2.08$ dex, as a standard for comparison with COS 171, since UMi 28104 has a metallicity close to our estimate of the pre-existing [Fe/H]

prior to COS 171. The similarity of the atmospheric parameters of COS 171 and UMi 28104 also results in a mitigation of systematic measurement errors, from various effects, in a differential comparison of abundance ratios.

Where possible, we have applied non-LTE corrections for the abundance ratios in COS 171 relative to UMi 28104, based on a variety of currently available non-LTE studies. However, no non-LTE corrections were available for vanadium.

An abundance ratio plot of COS 171 over UMi 28104 shows the 0.7 dex Fe enhancement and clear enhancements of Si, Ca, and Cr in COS 171; mild or zero enhancements of C, Ti, Mn, Ni, and Co are present. However, O, Na, Mg, K, Sc, V, Cu, and Zn show no evidence of production between UMi 28104 and COS 171.

We have compared the composition of COS 171 with a variety of supernova nucleosynthesis predictions for a range of metallicities: low- and high-mass core-collapse SNe II; Chandrasekhar-mass SNe Ia; sub-Chandrasekhar-mass SNe Ia; and PISNe. We find, in particular, that the Mn/Fe and Ni/Fe abundance ratios in COS 171 can only be reproduced in low-metallicity sub-Chandrasekhar-mass SN Ia nucleosynthesis. Chandrasekhar-mass SNe Ia fail to reproduce the low Mn/Fe ratios, due to pre-explosion simmering and to efficient electron captures during the initial phase of the explosion, which increases the neutron excess and the yield of neutron-rich species like Mn. Furthermore, the low Ni/Fe, Cu/Fe, and Zn/Fe ratios suggest that the bulk of these elements were synthesized in incomplete-silicon-burning conditions, which indicates a relatively low-mass sub-Chandrasekhar SN Ia. Our best estimate for the mass of the WD SN Ia progenitor to COS 171, based on the predictions of the Bravo models, is $0.95\,M_\odot$.

We conclude that COS 171 shows direct evidence of sub-Chandrasekhar-mass SN Ia nucleosynthesis.

We find that in order to reproduce the COS 171 metallicity by adding a a single SN Ia event into the pre-existing UMi composition (near [Fe/H] $= -2.05$ dex), dilution with approximately $10^4\,M_\odot$ of hydrogen is required. Detailed calculations show that SNRs expanding into a warm interstellar medium, with a density near 1.0 cm^{-3}, must mix with $10^4\,M_\odot$ of the medium for the expansion velocity to reduce to the observed velocity dispersion of interstellar clouds and could naturally explain the measured [Fe/H] of COS 171.

In our favored scenario for the chemical evolution of UMi and formation of COS 171, as UMi ran out of gas and star formation in the galaxy drew to a close, a single, stochastic, low-metallicity sub-Chandrasekhar-mass SN Ia, with WD mass near $0.95\,M_\odot$, enriched roughly $10^4\,M_\odot$ of warm interstellar gas, all or part of which subsequently formed into a star-forming molecular cloud, resulting in the last few stars in UMi, including COS 171.

Appendix A
Chandrasekhar-mass DDT SN Ia Nucleosynthesis Yields

Tables 4–7, below, list element yields, in $M_\odot$, for the Chandrasekhar-mass SN Ia deflagration to the DDT models of Badenes et al. (2003, 2008b), computed using the codes of Bravo et al. (1996). The nuclear reaction rates were the same as in Bravo & Martínez-Pinedo (2012), with $\xi_{CO} = 1$ (see Martínez-Rodríguez et al. 2017 for the definition of this parameter). a, c, e, and f refer to models with different adopted

densities for the transition to detonation, as illustrated in Badenes et al. (2008b). These models did not take into account the pre-explosion simmering phase of Piro & Bildsten (2008), which increases the neutron excess, η, of the SN Ia explosion. The minimum η for models that include simmering (Piersanti et al. 2017) is approximately equivalent to half a solar metallicity, or $Z \sim 0.007$; thus, the yields indicated for the two most metal-poor DDT models below, at $Z = 0.00025$ and $Z = 0.0025$, are not expected to occur.

Table 4
Chandrasekhar-mass DDTa SN Ia Yields (in $M_\odot$)

Elem./Z	0.00025	0.0025	0.01	0.025	0.075
C	8.374e−04	8.609e−04	9.051e−04	8.993e−04	1.029e−03
N	7.814e−06	6.408e−06	4.633e−06	3.039e−06	1.980e−06
O	3.605e−02	3.821e−02	4.030e−02	4.288e−02	4.886e−02
Ne	4.248e−04	4.427e−04	4.392e−04	4.922e−04	5.899e−04
Mg	7.856e−03	7.094e−03	5.339e−03	3.712e−03	2.244e−03
Si	1.184e−01	1.234e−01	1.266e−01	1.277e−01	1.276e−01
S	8.607e−02	8.717e−02	8.742e−02	8.539e−02	7.448e−02
Ar	2.392e−02	2.356e−02	2.259e−02	2.092e−02	1.642e−02
Ca	2.957e−02	2.834e−02	2.593e−02	2.243e−02	1.457e−02
Sc	1.390e−06	1.391e−06	1.422e−06	1.457e−06	1.620e−06
Ti	4.263e−04	4.313e−04	4.049e−04	4.060e−04	3.612e−03
V	1.451e−05	2.396e−05	4.981e−05	8.901e−05	2.703e−04
Cr	1.121e−02	1.128e−02	1.100e−02	1.158e−02	2.459e−02
Mn	2.828e−03	4.257e−03	6.705e−03	9.710e−03	1.625e−02
Fe	1.002e+00	9.952e−01	9.805e−01	9.567e−01	8.719e−01
Co	1.765e−03	3.381e−04	7.553e−04	1.069e−03	1.484e−03
Ni	3.613e−02	3.669e−02	4.884e−02	7.480e−02	1.562e−01
Cu	1.506e−04	2.565e−05	5.102e−06	9.224e−06	4.019e−05
Zn	2.731e−04	2.382e−04	9.474e−05	1.250e−04	5.537e−04

Table 5
Chandrasekhar-mass DDTc SN Ia Yields (in $M_\odot$)

Elem./Z	0.00025	0.0025	0.010	0.025	0.075
C	1.742e−03	1.741e−03	1.826e−03	1.949e−03	2.511e−03
N	1.091e−05	8.898e−06	6.253e−06	4.161e−06	3.074e−06
O	8.146e−02	8.404e−02	8.869e−02	9.411e−02	9.773e−02
Ne	1.163e−03	1.145e−03	1.319e−03	1.360e−03	1.987e−03
Mg	2.070e−02	1.851e−02	1.445e−02	1.036e−02	5.979e−03
Si	1.886e−01	1.945e−01	2.000e−01	2.028e−01	1.957e−01
S	1.293e−01	1.300e−01	1.309e−01	1.306e−01	1.137e−01
Ar	3.549e−02	3.478e−02	3.331e−02	3.145e−02	2.455e−02
Ca	4.408e−02	4.228e−02	3.858e−02	3.415e−02	2.256e−02
Sc	1.387e−06	1.410e−06	1.444e−06	1.497e−06	2.019e−06
Ti	6.254e−04	6.199e−04	5.873e−04	5.748e−04	3.705e−03
V	1.482e−05	3.048e−05	6.799e−05	1.213e−04	3.156e−04
Cr	1.751e−02	1.762e−02	1.727e−02	1.730e−02	2.812e−02
Mn	2.879e−03	5.234e−03	9.075e−03	1.366e−02	2.052e−02
Fe	8.174e−01	8.098e−01	7.983e−01	7.842e−01	7.606e−01
Co	5.507e−04	2.814e−04	3.457e−04	4.273e−04	7.059e−04
Ni	2.423e−02	2.514e−02	3.080e−02	4.232e−02	8.574e−02
Cu	9.432e−06	1.996e−06	6.117e−06	1.553e−05	6.691e−05
Zn	1.530e−05	8.768e−06	3.095e−05	7.185e−05	4.404e−04

Table 6
Chandrasekhar-mass DDTe SN Ia Yields (in $M_{\odot}$)

Elem./Z	0.00025	0.0025	0.010	0.025	0.075
C	5.312e−03	5.217e−03	5.323e−03	4.847e−03	8.553e−03
N	1.525e−05	1.231e−05	9.141e−06	5.998e−06	1.006e−05
O	1.393e−01	1.415e−01	1.487e−01	1.451e−01	1.639e−01
Ne	4.547e−03	4.517e−03	4.668e−03	4.272e−03	6.427e−03
Mg	3.936e−02	3.527e−02	2.822e−02	1.901e−02	1.199e−02
Si	2.897e−01	2.952e−01	3.003e−01	2.887e−01	2.939e−01
S	1.953e−01	1.949e−01	1.944e−01	1.842e−01	1.665e−01
Ar	5.161e−02	5.029e−02	4.789e−02	4.306e−02	3.418e−02
Ca	6.153e−02	5.865e−02	5.351e−02	4.548e−02	2.992e−02
Sc	1.384e−06	1.420e−06	1.477e−06	1.609e−06	2.987e−06
Ti	7.020e−04	6.821e−04	6.351e−04	6.284e−04	3.726e−03
V	1.292e−05	3.257e−05	7.169e−05	1.296e−04	3.175e−04
Cr	1.639e−02	1.621e−02	1.575e−02	1.661e−02	2.739e−02
Mn	2.893e−03	4.986e−03	8.228e−03	1.242e−02	1.668e−02
Fe	5.361e−01	5.339e−01	5.295e−01	5.648e−01	5.390e−01
Co	2.581e−04	2.675e−04	3.000e−04	3.704e−04	6.158e−04
Ni	2.329e−02	2.433e−02	2.778e−02	3.507e−02	5.964e−02
Cu	2.275e−06	2.617e−06	1.338e−05	3.481e−05	1.226e−04
Zn	7.611e−06	1.025e−05	5.837e−05	1.300e−04	5.070e−04

Table 7
Chandrasekhar-mass DDTf SN Ia Yields (in $M_{\odot}$)

Elem./Z	0.00025	0.0025	0.010	0.025	0.075
C	9.439e−03	8.658e−03	1.159e−02	1.249e−02	1.802e−02
N	1.693e−05	1.377e−05	1.165e−05	1.328e−05	2.547e−05
O	1.709e−01	1.710e−01	1.893e−01	2.002e−01	2.078e−01
Ne	8.000e−03	7.387e−03	7.698e−03	7.198e−03	7.685e−03
Mg	4.985e−02	4.383e−02	3.663e−02	2.678e−02	1.506e−02
Si	3.306e−01	3.345e−01	3.584e−01	3.573e−01	3.485e−01
S	2.212e−01	2.182e−01	2.260e−01	2.209e−01	1.915e−01
Ar	5.758e−02	5.527e−02	5.319e−02	4.896e−02	3.707e−02
Ca	6.740e−02	6.293e−02	5.618e−02	4.815e−02	2.881e−02
Sc	1.387e−06	1.416e−06	1.518e−06	1.779e−06	3.276e−06
Ti	6.416e−04	6.233e−04	5.504e−04	5.270e−04	3.669e−03
V	1.098e−05	3.135e−05	6.722e−05	1.171e−04	3.013e−04
Cr	1.333e−02	1.343e−02	1.196e−02	1.221e−02	2.443e−02
Mn	2.921e−03	4.699e−03	7.090e−03	9.551e−03	1.299e−02
Fe	4.108e−01	4.206e−01	3.782e−01	3.845e−01	4.080e−01
Co	2.590e−04	2.705e−04	3.039e−04	3.573e−04	6.884e−04
Ni	2.337e−02	2.438e−02	2.771e−02	3.449e−02	5.710e−02
Cu	2.243e−06	2.862e−06	1.807e−05	5.209e−05	1.536e−04
Zn	7.965e−06	1.210e−05	7.915e−05	1.916e−04	5.437e−04

Appendix B
Sub-Chandrasekhar-mass SN Ia Nucleosynthesis Yields

In Tables 8–11 below, we give the element yields for the sub-Chandrasekhar-mass SN Ia models, computed by E. Bravo (private communication) and used in our analysis, which are the same as in Yamaguchi et al. (2015), where the nuclear network was solved in conjunction with the hydrodynamic evolution. The nuclear reaction rates were the same as in Bravo & Martínez-Pinedo (2012), with $\xi_{CO} = 1$ (see Martínez-Rodríguez et al. 2017 for the definition of this parameter).

The initial models for the supernova explosion code were carbon-oxygen WDs with a core temperature $T = 10^8$ K, built in equilibrium. The metallicity, Z, was encoded in the mass fraction of ^{22}Ne, according to Timmes et al. (2003), and there was a scaled, $Z/Z_{\odot}$, and uniform solar composition of stable isotopes with baryon number $A > 22$ added.

The detonation was initiated by incinerating instantaneously the central 0.016% of the WD mass and forcing the propagation of a burning wave at the sound velocity up to a fraction of 0.10%–0.15% of the WD mass, after which the detonation propagated self-consistently. Burning inside the shock front, associated with the detonation wave, was omitted.

The hydrodynamic evolution was followed up to a time $t > 100$ s, at which time only the weak nuclear interactions continued to alter the chemical composition. The yields provided in Tables 8–11 account for all radioactive decays with halftimes shorter than 10 Myr. The only remaining radio activities are negligible, e.g., ^{40}K.

Table 8
0.88 $M_\odot$ Sub-Chandrasekhar SN Ia Yields (in $M_\odot$)

Elem./Z	0.00025	0.0025	0.01	0.025	0.075
C	5.164e−03	5.167e−03	5.170e−03	5.148e−03	5.028e−03
N	6.051e−06	5.441e−06	4.852e−06	4.400e−06	4.102e−06
O	1.041e−01	1.068e−01	1.112e−01	1.153e−01	1.189e−01
Ne	3.609e−03	3.547e−03	3.496e−03	3.498e−03	3.702e−03
Mg	3.114e−02	2.828e−02	2.266e−02	1.654e−02	9.179e−03
Si	1.531e−01	1.572e−01	1.609e−01	1.626e−01	1.597e−01
S	9.769e−02	9.780e−02	9.874e−02	9.867e−02	8.860e−02
Ar	2.650e−02	2.576e−02	2.458e−02	2.280e−02	1.786e−02
Ca	3.333e−02	3.162e−02	2.879e−02	2.489e−02	1.613e−02
Sc	8.913e−07	9.088e−07	9.374e−07	1.047e−06	2.029e−06
Ti	4.380e−04	4.271e−04	3.981e−04	3.588e−04	2.702e−04
V	4.140e−06	1.441e−05	3.769e−05	6.605e−05	1.105e−04
Cr	1.188e−02	1.173e−02	1.122e−02	1.043e−02	8.422e−03
Mn	1.184e−04	1.751e−03	4.293e−03	7.216e−03	1.207e−02
Fe	4.128e−01	4.090e−01	4.057e−01	4.060e−01	4.201e−01
Co	9.950e−07	4.802e−06	3.575e−06	7.092e−06	8.623e−05
Ni	8.124e−05	4.168e−04	1.735e−03	4.773e−03	1.720e−02
Cu	8.800e−07	1.859e−06	1.197e−05	3.472e−05	8.641e−05
Zn	8.800e−07	7.718e−06	5.012e−05	1.120e−04	9.344e−05

Table 9
0.97 $M_\odot$ Sub-Chandrasekhar SN Ia Yields (in $M_\odot$)

Elem./Z	0.00025	0.0025	0.01	0.025	0.075
C	2.673e−03	2.673e−03	2.668e−03	2.646e−03	2.563e−03
N	5.214e−06	4.515e−06	3.761e−06	3.054e−06	2.355e−06
O	7.320e−02	7.532e−02	7.791e−02	8.045e−02	8.264e−02
Ne	1.414e−03	1.387e−03	1.365e−03	1.364e−03	1.463e−03
Mg	2.044e−02	1.830e−02	1.425e−02	1.003e−02	5.308e−03
Si	1.219e−01	1.254e−01	1.280e−01	1.291e−01	1.256e−01
S	7.818e−02	7.822e−02	7.912e−02	7.907e−02	7.123e−02
Ar	2.118e−02	2.055e−02	1.980e−02	1.852e−02	1.490e−02
Ca	2.635e−02	2.484e−02	2.293e−02	1.999e−02	1.331e−02
Sc	9.746e−07	9.997e−07	1.007e−06	1.061e−06	1.495e−06
Ti	3.605e−04	3.592e−04	3.375e−04	3.037e−04	2.307e−04
V	4.806e−06	1.185e−05	3.057e−05	5.261e−05	8.691e−05
Cr	8.849e−03	8.751e−03	8.337e−03	7.665e−03	6.192e−03
Mn	1.081e−04	1.294e−03	3.218e−03	5.301e−03	8.423e−03
Fe	5.995e−01	5.978e−01	5.903e−01	5.787e−01	5.464e−01
Co	9.889e−04	5.310e−05	2.814e−04	4.666e−04	8.119e−04
Ni	8.199e−03	8.242e−03	1.442e−02	2.923e−02	8.383e−02
Cu	1.015e−04	2.195e−05	7.503e−06	1.934e−05	4.863e−05
Zn	1.846e−04	1.921e−04	8.754e−05	1.471e−04	1.906e−04

Table 10
1.06 $M_\odot$ Sub-Chandrasekhar SN Ia Yields (in $M_\odot$)

Elem./Z	0.00025	0.0025	0.01	0.025	0.075
C	1.453e−03	1.445e−03	1.432e−03	1.409e−03	1.346e−03
N	4.559e−06	3.716e−06	2.895e−06	2.281e−06	1.678e−06
O	4.123e−02	4.443e−02	4.779e−02	4.972e−02	5.100e−02
Ne	6.186e−04	6.101e−04	6.010e−04	6.002e−04	6.494e−04
Mg	1.017e−02	9.263e−03	7.123e−03	4.852e−03	2.452e−03
Si	8.820e−02	9.143e−02	9.410e−02	9.432e−02	9.004e−02
S	6.102e−02	5.997e−02	5.939e−02	5.866e−02	5.256e−02
Ar	1.732e−02	1.623e−02	1.503e−02	1.409e−02	1.187e−02
Ca	2.231e−02	2.000e−02	1.732e−02	1.510e−02	1.038e−02
Sc	1.104e−06	1.091e−06	1.110e−06	1.137e−06	1.317e−06
Ti	3.003e−04	2.994e−04	2.827e−04	2.570e−04	1.961e−04
V	4.999e−06	9.989e−06	2.554e−05	4.399e−05	7.216e−05
Cr	7.209e−03	7.170e−03	6.847e−03	6.334e−03	5.179e−03
Mn	1.123e−04	1.041e−03	2.625e−03	4.440e−03	8.340e−03
Fe	7.882e−01	7.874e−01	7.767e−01	7.570e−01	6.952e−01
Co	1.417e−03	1.491e−04	4.509e−04	6.932e−04	7.318e−04
Ni	1.145e−02	1.158e−02	2.164e−02	4.455e−02	1.244e−01
Cu	1.220e−04	2.539e−05	4.476e−06	9.157e−06	2.098e−05
Zn	2.385e−04	2.216e−04	7.440e−05	1.039e−04	1.256e−04

Table 11
1.15 $M_\odot$ Sub-Chandrasekhar SN Ia Yields (in $M_\odot$)

Elem./Z	0.00025	0.0025	0.01	0.025	0.075
C	7.354e−04	7.340e−04	7.319e−04	7.233e−04	6.917e−04
N	3.312e−06	2.970e−06	2.415e−06	1.918e−06	1.430e−06
O	2.028e−02	2.089e−02	2.180e−02	2.248e−02	2.301e−02
Ne	2.353e−04	2.320e−04	2.311e−04	2.340e−04	2.651e−04
Mg	4.516e−03	3.949e−03	2.890e−03	1.875e−03	9.078e−04
Si	5.642e−02	5.769e−02	5.911e−02	5.960e−02	5.784e−02
S	3.969e−02	3.966e−02	3.984e−02	3.929e−02	3.444e−02
Ar	1.106e−02	1.081e−02	1.040e−02	9.743e−03	7.778e−03
Ca	1.374e−02	1.317e−02	1.216e−02	1.072e−02	7.203e−03
Sc	1.204e−06	1.162e−06	1.179e−06	1.189e−06	1.258e−06
Ti	2.178e−04	2.196e−04	2.073e−04	1.849e−04	1.317e−04
V	4.644e−06	7.757e−06	1.984e−05	3.393e−05	5.454e−05
Cr	5.163e−03	5.171e−03	4.959e−03	4.579e−03	3.930e−03
Mn	1.021e−04	7.557e−04	1.957e−03	3.313e−03	9.813e−03
Fe	9.726e−01	9.718e−01	9.570e−01	9.280e−01	8.413e−01
Co	1.525e−03	2.890e−04	6.190e−04	8.838e−04	6.237e−04
Ni	1.387e−02	1.503e−02	2.916e−02	6.072e−02	1.579e−01
Cu	1.076e−04	2.199e−05	2.902e−06	4.689e−06	8.404e−06
Zn	2.257e−04	1.878e−04	5.592e−05	6.754e−05	7.518e−05

ORCID iDs

Carles Badenes https://orcid.org/0000-0003-3494-343X
Eduardo Bravo https://orcid.org/0000-0003-0894-6450

References

Arnett, W. D. 1971, ApJ, 166, 153
Asplund, M., Grevesse, N., Sauval, A.J., & Scott, P. 2009, ARAA, 47, 481
Asplund, M. 2005, ARA&A, 43, 481
Asvarov, A. I. 2014, A&A, 561, A70
Badenes, C., Bravo, E., Borkowski, K. J., & Domínguez, I. 2003, ApJ, 593, 358
Badenes, C., Bravo, E., & Hughes, J. P. 2008a, ApJ, 680, 33
Badenes, C., Hughes, J. P., Cassam-Chenaï, G., & Bravo, E. 2008b, ApJ, 680, 1149
Badenes, C., Maoz, D., & Draine, B. T. 2010, MNRAS, 407, 1301
Barklem, P. S., Christlieb, N., Beers, T. C., et al. 2005, A&A, 439, 129
Bergemann, M. 2011, MNRAS, 413, 2184
Bergemann, M., & Cescutti, G. 2010, A&A, 522, 9
Bergemann, M., Collet, R., Amarsi, A. M., et al. 2016, ApJ, submitted (arXiv:1612.07355)
Bergemann, M., & Gehren, T. 2008, A&A, 492, 823
Bergemann, M., Lind, K., Collet, R., Magic, Z., & Asplund, M. 2012, MNRAS, 427, 27
Bergemann, M., Pickering, J. C., & Gehren, T. 2010, MNRAS, 401, 1334
Bravo, E. 2013, A&A, 550, 24
Bravo, E., & Martínez-Pinedo, G. 2012, PhRvC, 85, 055805
Bravo, E., Tornambé, A., Domínguez, I., & Isern, J. 1996, A&A, 306, 811
Cescutti, G., & Kobayashi, C. 2017, A&A, 607, A23
Chamulak, D. A., Brown, E. F., Timmes, F. X., & Dupczak, K. 2008, ApJ, 677, 170
Chevalier, R. A. 1974, ApJ, 188, 501
Cioffi, D. F., McKee, C. F., & Bertschinger, E. 1988, ApJ, 334, 252
Cohen, J. G., & Huang, W. 2010, ApJ, 719, 931
Collet, R., Asplund, M., & Thévenin, F. 2005, A&A, 442, 643
Dave, P., Kashyap, R., Fischer, R., et al. 2017, ApJ, 841, 58

Fink, M., Hillebrandt, W., & Röpke, F. K. 2007, A&A, 476, 1133
Fulbright, J. P. 2000, AJ, 120, 1841
Hartwick, F. D. A. 1976, ApJ, 209, 418
Hasselquist, S., Shetrone, M., Smith, V., et al. 2017, ApJ, 845, 162
Heger, A., & Woosley, S. E. 2002, ApJ, 567, 532, (HW02)
Heger, A., & Woosley, S. E. 2010, ApJ, 724, 341
Iben, I., Jr., & Tutukov, A. V. 1984, ApJS, 54, 335
Ivanova, D. V., & Shimanskiĭ, V. V. 2000, ARep, 44, 376
Ji, A. P., Frebel, A., Simon, J. D., & Chiti, A. 2016, ApJ, 830, 93
Khokhlov, A. M. 1991, A&A, 254, 114
Kobayashi, C., Nomoto, K., & Hachisu, I. 2015, ApJL, 804, L24
Kobayashi, C., Umeda, H., Nomoto, K., Tominaga, N., & Ohkubo, T. 2006, ApJ, 653, 1145
Koch, A., McWilliam, A., Grebel, E. K., Zucker, D. B., & Belokurov, V. 2008, ApJL, 688, L13
Kozyreva, A., Yoon, S.-C., & Langer, N. 2014, A&A, 566, A146
Lawler, J. E., Sneden, C., Nave, G., et al. 2017, ApJS, 228, 10
Letarte, B., Hill, V., Tolstoy, E., et al. 2010, A&A, 523, A17
Mac Low, M. M., Burkert, A., & Ibáñez-Mejía, J. C. 2017, ApJL, 847, L10
Maeda, K., Röpke, F. K., Fink, M., et al. 2010, ApJ, 712, 624
Maoz, D., Mannucci, F., & Nelemans, G. 2014, ARA&A, 52, 107
Martínez-Rodríguez, H., Badenes, C., Yamaguchi, H., et al. 2017, ApJ, 843, 35
Martínez-Rodríguez, H., Piro, A. L., Schwab, J., & Badenes, C. 2016, ApJ, 825, 57
Mashonkina, L. 2013, A&A, 550, 28
Mashonkina, L., Sitnova, T., & Pakhomov, Y. 2016, AstL, 42, 606
Matteucci, F., & Brocato, E. 1990, ApJ, 365, 539
McWilliam, A., Rich, R. M., & Smecker-Hane, T. A. 2003, ApJL, 592, L21
Norris, J. E., Yong, D., Venn, K. A., et al. 2017, ApJS, 230, 28
North, P., Cescutti, G., Jablonka, P., et al. 2013, A&A, 541, 45

Osorio, Y., & Barklem, P. S. 2016, A&A, 586, 120
Piersanti, L., Bravo, E., Cristallo, S., et al. 2017, ApJL, 836, L9
Piro, A. L., & Bildsten, L. 2008, ApJ, 673, 1009
Reddy, B. E., Lambert, D. L., & Allende Prieto, C. 2006, MNRAS, 367, 1329
Sadakane, K., Arimoto, N., Ikuta, C., et al. 2004, PASJ, 56, 1041
Sbordone, L., Bonifacio, P., Buonanno, R., et al. 2007, A&A, 465, 815
Seitenzahl, I., & Townsley, D. 2017, in Handbook of Supernovae, ed. A. Alsabti & P. Murdin (Berlin: Springer)
Seitenzahl, I. R., Cescutti, G., Röpke, F. K., Ruiter, A. J., & Pakmor, R. 2013, A&A, 559, L5
Shen, K. J., Kasen, D., Miles, B. J., & Townsley, D. M. 2017, ApJ, submitted (arXiv:1706.01898)
Shetrone, M. D., Côté, P., & Sargent, W. L. W. 2001, ApJ, 548, 592
Shetrone, M. D., Venn, K. A., Tolstoy, E., et al. 2003, AJ, 125, 684
Shi, J. R., Gehren, T., Zeng, J. L., Mashonkina, L., & Zhao, G. 2014, ApJ, 782, 80
Sneden, C. 1973, ApJ, 184, 839
Takeda, Y., Hashimoto, O., Taguchi, H., et al. 2005, PASJ, 57, 751
Timmes, F. X., Brown, E. F., & Truran, J. W. 2003, ApJL, 590, L83
Van der Swaelmen, M., Hill, V., Primas, F., & Cole, A. A. 2013, A&A, 560, A44
Vázquez-Semadeni, E., Gómez, G. C., Jappsen, A. K., et al. 2007, ApJ, 657, 870
Venn, K. A., Shetrone, M. D., Irwin, M. J., et al. 2012, ApJ, 751, 102
Webbink, R. F. 1984, ApJ, 277, 355
Whelan, J., & Iben, I., Jr. 1973, ApJ, 186, 1007
Wood, M. P., Lawler, J. E., Sneden, C., & Cowan, J. J. 2014, ApJS, 211, 20
Woosley, S. E., & Weaver, T. A. 1995, ApJS, 101, 181
Yamaguchi, H., Badenes, C., Foster, A. R., et al. 2015, ApJL, 801, L31
Yan, H. L., Shi, J. R., Nissen, P. E., & Zhao, G. 2016, A&A, 585, 102
Yan, H. L., Shi, J. R., & Zhao, G. 2015, ApJ, 802, 36